The optical imaging system for non-destructively monitoring the manufacturing of tissue engineered vascular graft

By

CAI LI

DISSERTATION

Submitted in partial satisfaction of the requirements for the degree of

DOCTOR OF PHILOSOPHY

in

Materials Science and Engineering

in the

OFFICE OF GRADUATE STUDIES

of the

UNIVERSITY OF CALIFORNIA

DAVIS

Approved:

Laura Marcu, Chair

Subhash Risbud

Jeffery C. Gibeling

Alyssa Panitch

Committee in Charge

2021

The optical imaging system for non-destructively monitoring the manufacturing of tissue engineered vascular graft

Cai Li

Materials Science and Engineering

Abstract

Cardiovascular disease is the number one cause of death in the world. Vessel replacement with tissue engineered vascular graft (TEVG) is an available treatment for this type of diseases. Currently TEVGs are still under extensive investigation in terms of scaffold material selection and processing, graft maturating and recellularization strategies, and validation of graft functionality post implantation. The conventional measurements of TEVG properties are destructive, causing the studies of TEVG manufacturing to be expensive and time-consuming. In this dissertation, we built and examined a set of optical imaging tools for non-destructively monitoring TEVG properties to facilitate the development of TEVG.

In the first part, we report a multi-spectral fluorescence lifetime imaging (FLIm) device that measures the tissue autofluorescence (e.g., collagen, elastin). We investigated the potential of using this device to non-destructively monitor the biochemical and biomechanical properties of the biomaterials used to develop TEVGs. This study has shown a strong correlation between the fluorescence parameters (lifetime, spectral ratio) and the results of conventional measurement (collagen content, Young's Modulus, ultimate tensile strength), and has demonstrated the capability of FLIm to help inform about scaffold material selection and processing.

In the second part, we report the design and engineering of a bioreactor where the TEVG can be cultured *in situ* under a controlled environment and pulsatile flow that simulates

physiological conditions. In this study, we adopted the FLIm device for *in situ* imaging of the intraluminal surface of TEVG when cultured inside the bioreactor. In addition, an exogenous continuous wave (cw) fluorescence imaging modality was also incorporated in the FLIm device. To demonstrate its capability of *in situ* imaging inside the bioreactor, a TEVG was seeded with enhanced green fluorescence protein (eGFP) labeled human mesenchymal stem cells (hMSC) and mounted inside the bioreactor. The TEVG was then scanned with this FLIm and exogenous cw fluorescence imaging system. The presence of cells was captured by the FLIm image with cell seeded regions showing lower lifetime value, validated by the co-registered eGFP fluorescence image acquired simultaneously by our single system.

In the third part, we report the design and engineering of an intravascular multi-modal imaging approach combining FLIm and optical coherence tomography (OCT). The addition of OCT modality can provide a high-resolution 3D structural image of the TEVG. We demonstrated the system performance by imaging an antigen removed saphenous vein (SV) and successfully acquired both FLIm and OCT images of the intraluminal surface of SV, allowing a comprehensive assessment of graft biochemical and structural properties.

In summary, here we describe and discuss the three optical systems designed for non-destructive monitoring of the TEVG properties. Current findings show the potential of these optical systems as valuable tools to optimize and improve the manufacturing of TEVG.

Table of Contents

Chapter 1: Introduction

1.1 Tissue engineered vascular graft (TEVG)

1.1.1 Background

Cardiovascular disease is the number one cause of death in the world. Based on the report by World Health Organization in 2006, 23.3 million of global death will be associated with cardiovascular disease in 2030 [1]. Replacement of diseased vessel with the vascular graft made from autologous vessel is currently an available solution to the cardiovascular diseases. However, the use of autologous vascular graft has the problems such as limited availability, invasive harvest, and still shows a high failure rate of 50% in long term [2]. Therefore, researchers are looking for alternatives to the autologous vascular graft. Synthetic vascular graft made from polymer materials have shown excellent clinical performance for replacing large diameter vessels (>8 mm) and middle diameter vessels (6-8 mm) [3], [4], but are not suitable for replacing small diameter vessels (<6 mm) due to a poor patency rate found in long term [5]. Tissue engineered vascular grafts (TEVG) are currently considered as a good solution to this request of small diameter vascular grafts [6]. TEVG is a tissue conduit with the structure close to the native vessels including a supportive tubular tissue construct mimicking the media layer of vessels and an intact layer of endothelial cells on the lumen surface [7]. It can grow, remodel, and repair itself inside the human body and this capability of self-accommodation enables it to perform better for long time post implantation [6]. At present, there have been many different manufacturing techniques developed to produce TEVG of all types of size [6], [8]. In this dissertation, we will focus on discussing the fabrication process of TEVG designed for small diameter vessels (3-6 mm).

1.1.2 TEVG Manufacturing

Many different techniques have been developed to manufacture TEVG. They can be

categorized to: 1) Degradable scaffold based methods, 2) Decellularized natural matrix based methods and 3) Self-assembly process [6]. The scaffold-based methods produce the TEVG by culturing cells on scaffolds of tubular structure. The scaffolds are typically made from synthetic or natural polymer materials. During the culturing, the polymer scaffold is degraded, and the tubular tissue construct is formed by cells. This tubular tissue construct is then cultured *in vitro* inside a bioreactor for maturation. The bioreactor can provide a controlled environment with temperature, humidity, CO_2 level optimized for simulating the physiological conditions. It can also generate a biomimetic pulsatile flow to mechanically stimulate the TEVG, and studies showed that this stimulation can effectively improve the TEVG structural properties, mechanical properties and cell viability on the tissue constructs [9], [10]. Instead of growing tissues on a degradable scaffold, the decellularized natural matrix based methods directly harvest the tissue constructs from animals and remove the antigenic cellular materials using the process called decellularization. This avoids the immunological reactions in host after implanting this type of vascular graft. However, the decellularization may damage the extracellular matrix (ECM) and degrade the tissue structural and biochemical properties [11]. It is important to carefully design the decellularization process based on the natural matrix to use [12]. If the decellularization is performed appropriately, this type of vascular graft is featured with the inherent mechanical strength because of its naturally mature architecture. Another problem of this decellularized matrix based vascular graft is the lack of cellularity after implantation. This causes the damage or absence of an intact layer of endothelial cells, which functions as protecting the vascular graft from thrombosis or infections [13]. Studies showed that this poor cellularity can be combated by seeding the autologous cells and culturing *in vitro* inside the bioreactor before implantation. The

mechanical stimulation inside bioreactor can enhance the endothelial cell adhesion to the tissue construct [14], [15]. Unlike the previous two techniques, tissue engineering by self-assembly (TESA) does not require a degradable scaffold or natural tissue construct to start with. This method enables cell to grow ECM from scratch. The vascular structure is created by firstly producing sheets of cell and shaping them around mandrel to form the tubular shape [16], or generated by self-assembly of microtissue aggregates, or cell 3D printing technique [17], [18]. Like the scaffold based methods, after the tubular tissue construct is formed, it is cultured *in vitro* inside the bioreactor to improve its structural integrity and mechanical strength [19]. Researchers are still investigating these techniques to better manufacture TEVG in terms of 1) material selection and processing for forming the tubular tissue construct, 2) *in vitro* culturing and recellularization strategies before implantation, 3) robust and long-term clinical performance of the vascular graft. All TEVG studies require measuring the tissue structural properties, biochemical and biomechanical properties, and the cellularity to evaluate the quality of vascular graft during the manufacturing [6].

1.2 Conventional destructive measuring techniques for TEVG studies

To measure the properties of TEVG, many different measuring techniques are applied. The following sections will describe the current dominant methods applied in tissue engineering studies for measuring the tissue biochemical compositions, tissue morphology, biomechanical properties, and monitoring the recellularization process.

1.2.1 Biochemistry assays

Biochemistry assays are often used to quantitatively measure the compositions of extra-cellular proteins in TEVG. For example, the collagen content per dry weight in tissues can be measured using colorimetric hydroxyproline test [20]; the elastin concentration can be

measured using a competitive ELISA kit [21]. Both of these assays require the tissues to be lyophilized and digested before the quantitative measurements [20], [22]. And to improve the measurement precision, a large number of samples are required for statistical analysis [23].

1.2.2 Histology

Histology is a measurement of biochemical composition and structural properties by visualizing the tissue morphology and highlighting specific proteins or cells using labeling dyes [22]. To make the histological analysis, tissues are stained with dyes like Hematoxylin and Eosin (HE), Verhoeff Van Gieson (VVG), to label the components like collagen, elastin, or cell nuclei so they can show different colors in microscope images. During the process, the tissues are fixated, dehydrated, embedded, sectioned, stained and finally mounted on a microscope slide for imaging [24].

1.2.3 Mechanical tests

Different mechanical tests are applied for the development of TEVG. At the stage of material selection and processing, the tensile properties of the fabricated tissue constructs are determined by a uniaxial tensile tester [22]. After tissues being shaped to the tubular structure and cultured inside the bioreactor, the burst pressure can be measured by pressurizing the flow and measuring the minimum pressure that results in the failure [25]. In addition, other tests like compliance test, suture retention test, fatigue tests and vessel ringlet pull test can also be applied to examine TEVG mechanical performances before implantation [25].

1.2.4 Labeled fluorescence imaging

The formation of an intact layer of endothelial cells is important and should be monitored during the manufacturing. The endothelium layer can prevent the implanted TEVG from failures caused by inflammation, thrombosis, or vascular smooth muscle cell proliferation

[26]. Fluorescent labels like green-fluorescent protein (GFP) and carbocyanine are often used to tag the cells [27], [28] and the cellular performance can then be studied by imaging them using the fluorescence microscope. However, none of these fluorescent labels are approved for clinical use due to the potential toxicity [29], [30]. So, these labels cannot be added to the TEVG for clinical studies.

1.3 Non-destructive measuring techniques for TEVG studies

The biggest drawback of these conventional techniques is that the samples will be discarded after measurements. This gives rise to two problems: 1) Research and Development (R&D) requires many samples and animals, making the studies very time-consuming and costly; 2) Quality control is difficult since the graft for implantation cannot be measured using these techniques. Therefore, it is worthwhile developing a non-destructive measuring technique for TEVG applications to monitor the grafts' structural and biochemical properties.

1.3.1 Non-optical imaging modalities

Clinical imaging modalities like computed tomography (CT) with or without angiography (CT(A)), magnetic resonance imaging (MRI), F-fluoro-D-deoxyglucose positron emission tomography (F-FDG-PET), have been used to monitor vascular graft patency rate after implantation [31]–[33]. In addition, magnetic resonance elastography (MRE) was adapted to characterize the stiffness of vascular graft *in vivo* by capturing the cyclic displacements of small amplitude [34]. Micro-CT was used to visualize the 3D structure of ECM without the need of staining [35]. However, these techniques require very expensive instruments, which is not suitable for *in vitro* studies of TEVG.

Acoustic imaging is potentially useful for non-destructive monitoring of the TEVG properties by imaging the tissue anatomical structures [36]. The development of intravascular ultrasound

(IVUS) imaging makes it a good tool for imaging tubular tissue construct like vascular grafts. It has been applied for both *ex vivo* and *in vivo* studies to monitor the structural changes in vessels [37], [38]. Researchers are also developing advanced signal processing algorithms and modifying instrument hardware to measure other properties like cell density and mechanical properties [39]. However, the robustness of these parametric analyses is still under investigation and the assumptions in these algorithms need to be carefully examined for accurate measurements [40]. In addition, the resolution of acoustic imaging is over 100 micron, limiting the application of using it to study TEVG structural properties [41].

1.3.2 Optical imaging modalities

Optical imaging techniques acquire the contrasts from the light tissue interactions [42]. The benefits of applying optical imaging for tissue engineering include low cost, decent resolution, excellent sensitivity and specificity, and ease of use for *ex vivo* and *in vivo* measurements [43]. Various optical imaging systems have been developed and investigated for measuring vascular grafts. For example, optical coherence tomography (OCT) that measures the echo time delay of reflected light using low coherence interferometry, has been used for structural assessment of vascular grafts inside the bioreactor and autologous vein graft after implantation [44]–[46]. Nonlinear imaging based on effects like second harmonic, or third harmonic generation, has been utilized to visualize the spatial distribution of biochemical components like elastin and collagen [47], [48]. Fluorescence imaging by measuring the spontaneous emission from natural fluorophores in tissues, has been widely used to characterize the tissue biochemical and biomechanical properties [49], [50]. Different optical imaging techniques can also be combined in a single system to comprehensively analyze the tissue properties [51], [52].

1.4 Objectives

In this dissertation, we reviewed, designed, assembled, and evaluated a variety of fiber based optical imaging systems suitable for monitoring different stages of TEVG manufacturing including materials selection and processing, maturation inside the bioreactor, and validation of clinical performance.

In chapter two, a fiber based multi-spectral fluorescence lifetime imaging system (FLIm) is described. Its sensitivity to the tissue biochemical and biomechanical properties was explored using a pairwise comparison study by measuring the same tissues samples of different properties with FLIm and conventional measurements. Statistical analysis was performed to evaluate the correlation between the optical imaging parameters and conventional measurement results. This study is to investigate the potential of using FLIm to non-destructively monitor biochemical and biomechanical properties of biomaterials used to manufacture TEVGs.

In chapter three, a fiber based multi-modal optical system combining FLIm and exogenous continuous wave (cw) fluorescence imaging modality was described. A reciprocal scanning system and a side viewing imaging probe were fabricated to adapt this multi-modal system for *in situ* imaging of TEVG inside a bioreactor. To evaluate the system performance, a TEVG was seeded with enhanced green fluorescence protein (eGFP) labeled human mesenchymal stem cells (hMSC) and mounted inside the bioreactor. The TEVG was then scanned with this FLIm and exogenous cw fluorescence imaging system to demonstrate the system sensitivity of assessing the recellularization process.

In chapter four, the study is to develop a multi-modal optical imaging system suitable for *in vivo* studies that can provide both biochemical and structural properties of TEVG. The design and engineering of an intravascular fluorescence lifetime imaging (FLIm) and optical

coherence tomography (OCT) was described. The system performance was optimized by successfully building a motor drive unit that realizes a high and stable throughput for light coupling, and a catheter using the reflective micro-optic that produces high quality beam profiles for both UV and IR light. The system performance was demonstrated by imaging a tubular fluorescent phantom and an antigen removed saphenous vein.

Chapter 2: Optical imaging system for non-destructively monitoring properties of vascular graft materials

2.1 Introduction

2.1.1 Optical Imaging systems for measuring tissue properties

During the fabrication of TEVG, it is essential to produce an Extracellular matrix (ECM) with appropriate biochemical composition and biomechanical strength [6]. ECM is a complex, 3D environment that plays a key role in determining the structure and function of tissues and organs. As discussed in chapter one, an optical imaging system capable of non-destructively characterizing tissues' properties is highly valuable for TEVG applications. Plenty of studies were conducted to explore the potential of different optical modalities for quantitatively monitoring the extracellular biochemical components (e.g., collagen, elastin) and mechanical properties. For example, one of the sub-modalities of OCT, polarization sensitive OCT, is capable of quantifying collagen content by measuring the tissue birefringence [53]. In addition, optical coherence elastography (OCE), is capable of quantitatively measuring tissue mechanical properties [54]. However, an independent loading system is required for performing OCE measurement, which increases the cost and complexity of this approach. Another study demonstrated the possibility of utilizing second harmonic generation (SHG) signal and two photon excitation fluorescence (TPEF) to predict the compositional and mechanical changes of ECM after myocardial infarction [55]. The study showed that the SHG and TPEF signals were correlated with the collagen content and elastic moduli of the ECM. Although the longer excitation wavelength used in SHG/TPEF and the nonlinear dependence of absorption as a function of intensity allows for deeper penetration and 3D sectioning capabilities, the cost and complexity of fiber-based multiphoton imaging mean that it is not well suited to widespread use as a tool for evaluating tissue constructs *in vitro*. Previous work

in our group also showed that a Raman spectroscopic imaging can be used to study collagen crosslinking and calcification process. The study found that the Raman bands at 856 cm^{-1} for hydroxyproline and at 1032 cm^{-1} for hydroxy-pyridinium show a strong correlation with pyridinium crosslinks and the characteristic hydroxyapatite bands at 959 and 1038 cm^{-1} can be used to indicate the calcified regions [56]. However, the Raman spectroscopic measurements are typically slow due to the extremely low yield of Raman scattering. Although the development of Stimulated Raman Scattering (SRS) improves the imaging speed, it compromises the number of spectral bands to collect and largely increases the cost of system [57].

2.1.2 Tissue autofluorescence

Fluorescence is a physical phenomenon that some substances emit photons after absorbing excitation light. The mechanism of this photophysical process can be well demonstrated by Jablonski diagram (Fig. 1). Before excitation, molecule is generally in the lowest vibration level of the ground state S_0. When the excitation photon energy is higher than the band gap between ground state S_0 and excited state S_1, molecule can absorb the photon energy and is excited to an electronically excited singlet state. For each electronic state, there are vibrational sublevels corresponding to different molecular geometries distorted with respect to the lowest energy vibrational mode. In the absorption process, molecule is excited to one of the vibrational levels of the excited singlet state depending on the excitation photon energy. The absorption spectrum reflects the probability distribution of transitions from

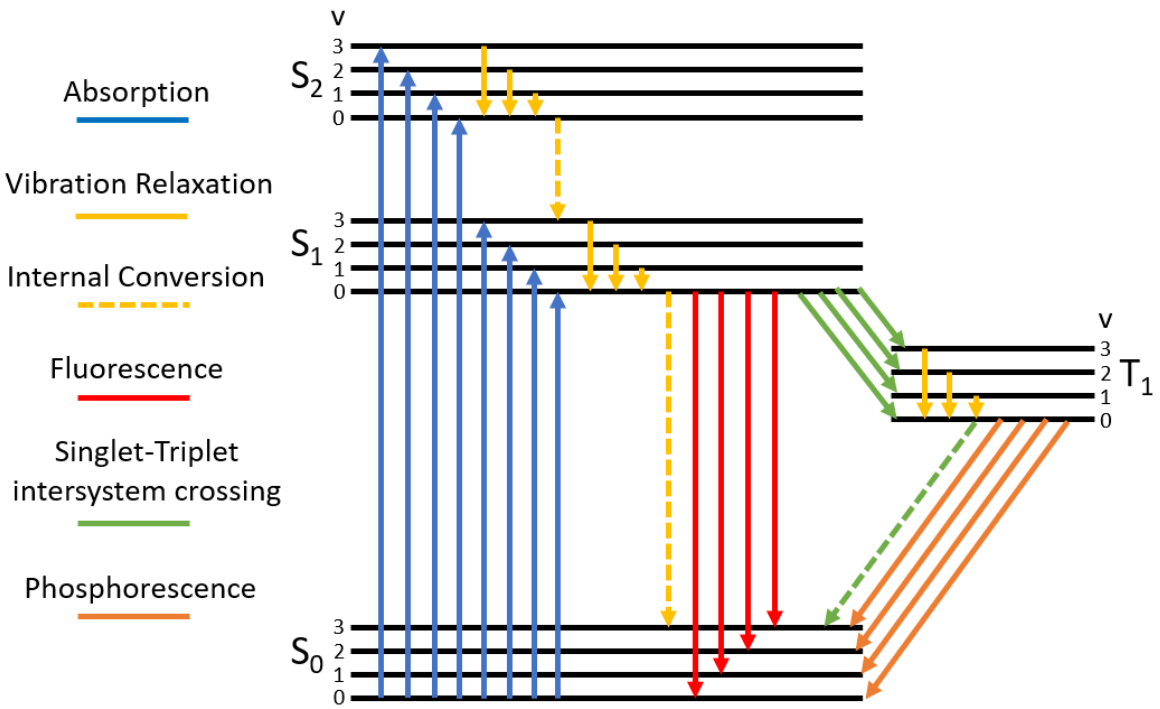

Figure 1. Jablonski diagram showing the photophysical processes of molecules.

ground state to these different vibrational levels in the excited electronic states. Molecule at the excited state is not stable and tends to release the excitation energy. It will first return to the lowest vibrational level of the S_1 electronic state through vibrational relaxation and internal conversion. And fluorescence occurs when molecule further decays to the ground state by radiation. Like the absorption spectrum, the emission spectrum reflects the probability distribution of transitions from the lowest vibrational level of S_1 state to different vibrational levels in the ground state. However, there are other processes like internal conversion, intersystem crossing, and phosphorescence that also allow molecule decay to the ground state. The fluorescence emission is the second slow process (10^{-9} s) among all these transitions (Absorption: 10^{-15} s, Vibration Relaxation: 10^{-14} - 10^{-12} s, Internal Conversion: 10^{-12} s, Intersystem crossing: 10^{-14} s, Phosphorescence: 10^{-5} - 10s). The time resolved fluorescence is measuring the temporal dynamic of the fluorescence emission and the fluorescence lifetime is a parameter that quantitatively describes the speed of measured

fluorescence decay. The absorption spectrum, emission spectrum as well as fluorescence lifetime can be measured to characterize the fluorescence light that is associated with tissue chemical composition. Structural proteins like collagen, elastin, are fluorescent under ultraviolet (UV) excitation [58]. Many studies have demonstrated the value of measuring these natural fluorophores which exist natively in tissues or cells to non-destructive monitor their property changes. For example, Lewis et al. demonstrated a correlation between endogenous autofluorescence (AF) measured with a spectrofluorometer and biomechanical stiffness, and suggested using the endogenous UV fluorescence intensity as a biomarker for monitoring the functional state of tissues [58]. In addition, previous studies in our group have demonstrated that fluorescence lifetime imaging is a powerful tool for label-free monitoring of the state of biological tissues like porcine articular cartilage and cardiovascular tissues [59]. Moreover, fluorescence lifetime is highly sensitive to the fluorophore microenvironment that is associated with the molecular structure of tissues [60].

2.1.3 Multi-spectral fluorescence lifetime imaging (FLIm)

The multi-spectral fluorescence lifetime imaging (FLIm) system developed in previous work is capable of simultaneously detecting the changes in spectral emission and fluorescence lifetime of unlabeled tissue samples in distinct wavelength bands [61]. In the rest of chapter, we use FLIm to non-destructively assess changes in the composition and mechanical properties of native bovine pericardium (BP) following partial digestion of the matrix using bacterial collagenase. BP is a biomaterial that is well known for fabricating TEVG. We compared FLIm measurements with the results of hydroxyproline assays, for collagen content, and tensile testing, for Young's Modulus and Ultimate tensile strength (UTS) estimation, at different levels of collagenase digestion. The FLIm system's sensitivity was

calibrated by performing pairwise correlation analysis between the fluorescence parameters and conventional measurement results. In addition, we also studied the effect of solvent polarity to explain the observed changes of emission spectrum and lifetime. The following section is adapted from our previous work [62], with the approval from *Annals of Biomedical Engineering*.

2.2 Multi-spectral fluorescence imaging system for non-destructively monitoring collagenase digestion of bovine pericardium

2.2.1 System description

The schematic of the FLIm system is shown in Fig. 2. Excitation is performed by a 355 nm UV pulsed laser (STV-02E, TEEM photonics, France), the light from which is guided to the sample using a 2 m long, 400 μm core flexible multimode optical fiber (Polymicro Technologies, Phoenix, AZ). Sample fluorescence is collected using the same fiber optic. A custom wavelength selection module (WSM) including dichroic beam splitters and bandpass filters is used to divide the autofluorescence into three distinct spectral bands (Channel 1: 390/18 nm, Channel 2: 435/40 nm, Channel 3: 510/84 nm). Each spectral band has its own fiber optic delay line, used to temporally multiplex the light from the three spectral bands onto a single micro channel plate photomultiplier tube (MCP PMT) detector. The fluorescence dynamics are recorded using a high-speed digitizer operating at the sampling rate of 12.5 GS/s (PXIe-5185, National Instruments, Austin, TX). Fluorescence intensity is calculated by integrating the recorded fluorescence decay. Intensity ratios of each spectral channel are

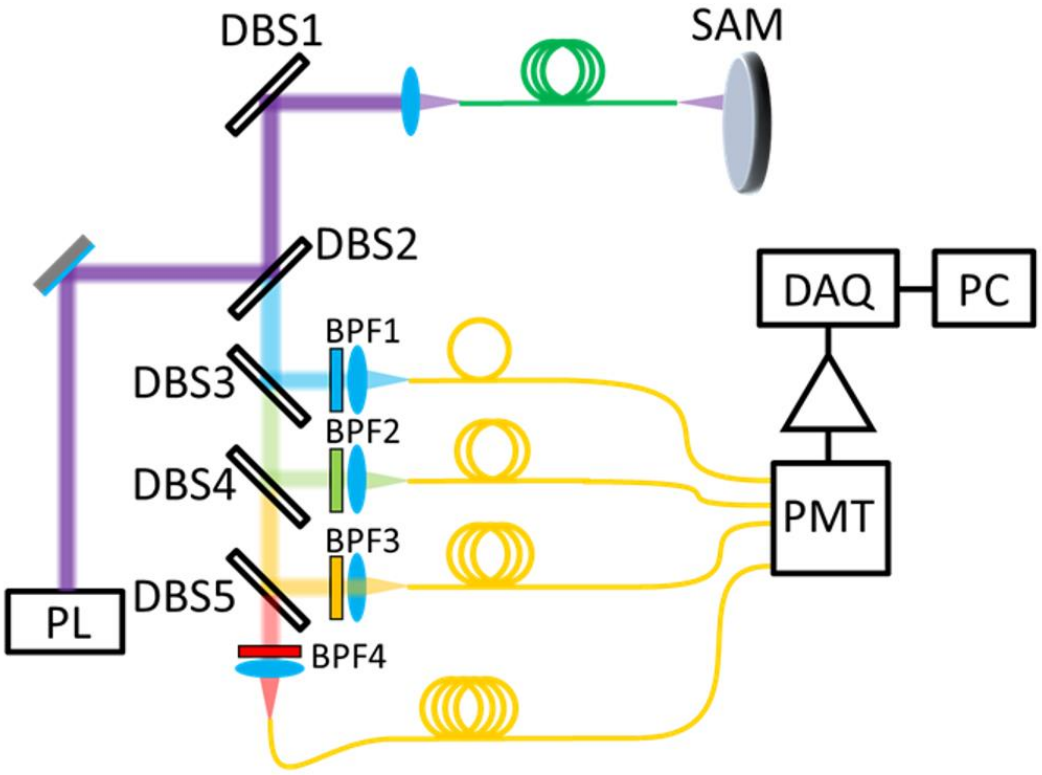

Figure 2. schematic of the fiber based FLIm system architecture. PL: 355 nm pulsed laser, DBS: dichroic beam splitters, BPF: bandpass filter, PMT: photomultiplier tube, DAQ: data acquisition module, PC: personal computer, SAM: biological sample.

obtained by dividing that channel's intensity over the sum of all channels' intensities. The average fluorescence lifetime is calculated as the expectation value of the probability density function of the decay. The temporal instrument response function is deconvolved from the raw fluorescence decay using a constrained least square deconvolution with Laguerre expansion [63]. The spatial distribution of fluorescence intensity and lifetime is measured by raster scanning the fiber optic distal tip across the sample surface using a 3-axis translation stage (MT S50-Z8, Thorlabs, Newton, NJ).

2.2.2 Materials and Methods

2.2.2.1 Sample Preparation

To test the system performance, a collagenase digestion experiment was designed. The

biomaterial we used for the experiment is bovine pericardium, a collagen rich material harvested from young adult cattle. The materials were ordered from Spear Products, Coopersburg, PA. Following removal of connective tissue and pericardial fat, the tissue was trimmed and cut into strips that were frozen in Dulbecco's Modified Eagle Medium (DMEM) with 15% (v/v) dimethyl sulfoxide (DMSO) at -80 ˚C. Samples used in the experiment were thawed, then washed in phosphate-buffered saline (PBS), pH 7.4, for 30 min, and finally cut to small round discs using 5 mm biopsy punches. For consistency, the control and digested groups were through the same procedure and all the samples were harvested from the same batch.

Samples were divided into two groups: control and digested. Control samples were placed in 2 ml Hank's Balanced Salt Solution (HBSS), and digested samples were placed in 2 ml 200 U ml^{-1} Clostridium histolyticum collagenase type I (Gibco, Carlsbad, CA) diluted by HBSS. Samples were incubated at 37 ˚C for 0, 8, 16 or 24 hours, and then washed at room temperature with phosphate buffered saline (PBS). The digestion exposure time of samples for tensile test (0, 8, 12 hours) were different from the ones used in other tests because the samples after 16 hours became too soft to be transported to the measuring stage without any damage. To remove the residual collagenase and fiber debris before measuring, all the samples were rinsed in PBS for 5 min, then washed with fresh PBS on a shaker for 24 hours, and rinsed with fresh PBS again for 5 min. After washing, samples were subjected to tensile testing, hydroxyproline assay, and histology. Samples tested for tension and collagen content were previously imaged with the FLIm system. All digestion experiments were conducted with N = 6 per group per time point.

2.2.2.2 Biochemistry assays

Collagen content of BP samples were determined as previously described (N = 6 samples per time point) [12]. Samples were weighed [wet weight (WW)], lyophilized for 72 hours and weighed again [dry weight (DW)]. Lyophilized samples were digested in 5N HCl (1 ml per 10 mg DW) at 120 ˚C for 24 hours. Bovine collagen type I (Chondrex Inc., Redmond, WA) was digested similarly and served as a reference. Sample collagen content per DW was quantified using collagen I standards and a Hydroxyproline Assay Kit (Chondrex Inc., Redmond, WA).

2.2.2.3 Mechanical tests

Tensile testing was conducted using a uniaxial material testing machine (Test Resources, Shakopee, MN), as previously described [12]. After FLIm measurements, BP samples were cut into dog-bone shaped tensile specimens parallel to the primary collagen fiber direction. Sample thickness and width were measured via ImageJ software (NIH, Bethesda, MD). A uniaxial strain to failure test was conducted with a fixed gauge length of 1.5 mm and a strain rate of 1% of the gauge length per second. For each sample, load-displacement curves were normalized to specimen cross- sectional area. The apparent Young's Modulus was calculated by least squares fitting the linear portion of the resulting stress-strain curve in MATLAB v2018a (MathWorks Inc., Natick, MA) while the UTS was defined at the maximum stress.

2.2.2.4 Histology

Formalin-fixed, paraffin-embedded 5 mm biopsy punches of control and digested samples (N = 6 per group per time point) were histologically processed for hematoxylin and eosin (HE) and PicroSirius Red (PSR) staining, according to standard procedures. Image were captured using Aperio ScanScop and processed using ImageScope software 12.3.2.5030 (Leica

Microsystems Inc., IL, USA). HE staining was used to assess general tissue morphology, and PSR staining was used to specifically visualize collagen fiber structures.

2.2.2.5 Statistical analysis

Kruskal Wallis H test was performed to compare the mean intensity ratios and fluorescence lifetime of all the control and digested groups. The difference between the control and digested groups were analyzed using Mann Whitney U test and quantified by calculating the unstandardized mean difference. The Kendall τ_B correlation analysis was performed for analyzing the ordinal correlation between FLIm results (intensity ratio, lifetime) and conventional measurement results (collagen content, Young's modulus, UTS). The statistical analysis was performed using Matlab v2016a and RStudio.

2.2.3 Results

2.2.3.1 Conventional measurement results

The effect of collagenase degradation is shown in Fig. 3. HE staining was used as the gold standard for imaging tissue morphology and demonstrated that collagenase resulted in the degradation of ECM components. Fewer fiber structures remained were observed in the tissue samples after long digestion times (Fig. 3a). In terms of collagen density, PSR staining, which specifically stains collagen in red, showed that after 8 hours digestion, wavy collagen fibers were still present; however, the distance between fibers became much larger and fibers were noticeably thinner than in native tissue. Following 16 hours digestion, the fibers started to disassemble in fibrils. After 24 hours, collagen disruption was more severe and only small wavy fibers were observed with markedly disrupted organization (Fig. 3b). The lightening of PSR staining image also indicate the decrease of collagen content during collagenase degradation.

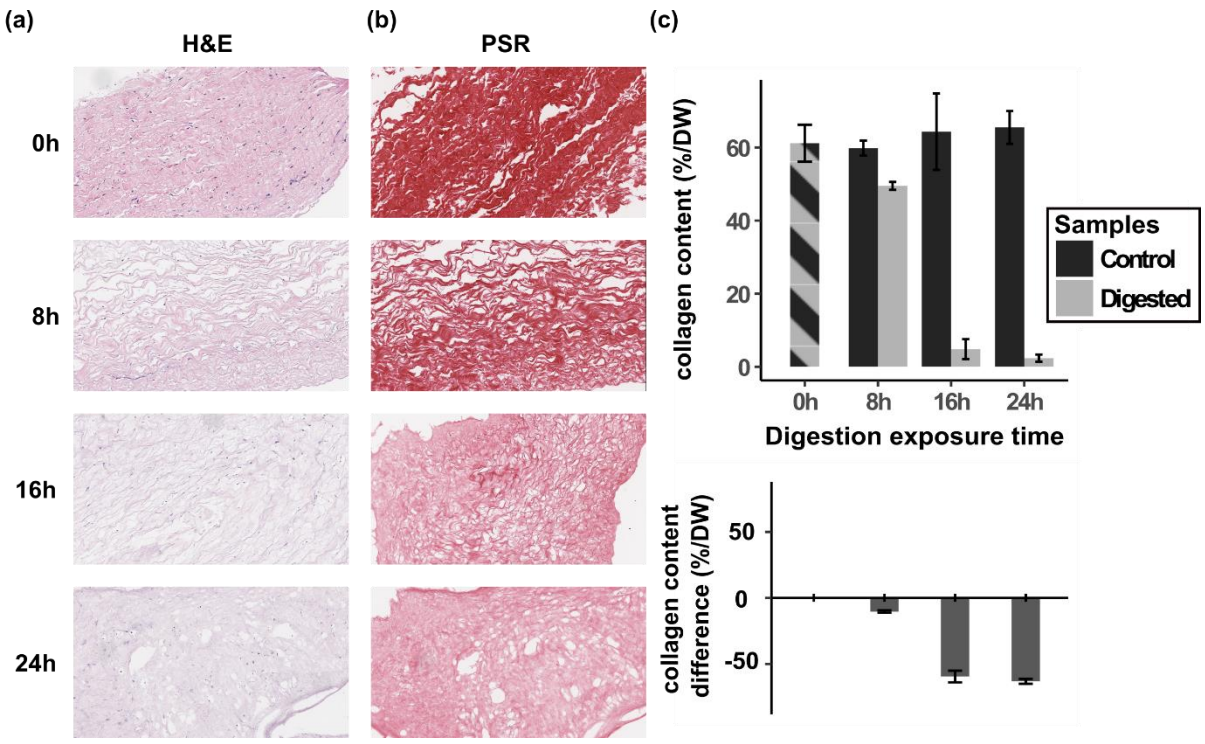

Figure 3. Histology and collagen measurements over different digestion exposure times. Hematoxylin and eosin staining (HE) and (b) PicroSirius Red staining (PSR) of digested group at 0, 8, 16, 24 h time points; (c) Collagen content measured with hydroxyproline assay (above) and the unstandardized difference between the control group and digested group (below) over different digestion exposure time. Hatch pattern represents that the digested group and control group are from same samples.

Quantitative analysis of collagen content was performed using hydroxyproline assay. As shown in Fig. 3c, collagen content of the digested group decreased dramatically over the time course of collagen degradation (63.14 ± 1.87% reduction in collagen content per DW after 24 hours), while the control group remained constant. The decrease of collagen content for the digested group compared to the control group is shown to be associated with digestion exposure time.

Since collagen is the dominant ECM structural protein in BP, collagen degradation and removal results in a considerable change of the biomaterial mechanical properties. As demonstrated by tensile testing, the digested group became softer after collagenase degradation. Both of Young's Modulus and UTS of the digested group became smaller with

digestion exposure time, while the control group did not show significant variation (Table. 1). To be noticed, the mechanical strength decreased dramatically after 8 hours digestion even when most of the collagen content remained. This nonlinearity between the changes of mechanical properties and collagen content may be due to the damage of the collagen matrix structure at the early stage of collagenase degradation.

Table 1. Young's modulus and UTS of the control and digested groups at 0, 8, 12h time points

Digestion exposure time (hours)	Young's Modulus (MPa)		UTS (MPa)	
	Control	Digested	Control	Digested
0	3.09 ± 1.52	3.13 ± 0.82	1.65 ± 0.52	1.77 ± 0.40
8	3.00 ± 1.04	0.03 ± 0.03	1.66 ± 0.38	0.05 ± 0.03
12	3.38 ± 0.63	0.02 ± 0.03	1.29 ± 0.44	0.03 ± 0.02

2.2.3.2 FLIm results

Intensity ratio and fluorescence lifetime maps recorded in Channel 1 (390/18 nm) for the digested group at different time points are shown in Fig. 4. As mentioned above, the intensity ratio is defined as an indicator of fluorescence spectra. Both fluorescence spectra and fluorescence lifetime can be used for analyzing the compositional change in BP. A clear continuous decrease is found for both the intensity ratio and fluorescence lifetime in Channel 1. Given the homogeneity of the sample, a circular region of interest (ROI) for each sample was manually selected (black circles in Fig. 4) and data in each channel within the ROI were analyzed. Channel 3 (510/84 nm) will not be discussed further because very low correlation was found with the conventional measurement results.

The statistical analyses were done for 6 control and 6 digested groups at digestion exposure time 0, 8, 16 and 24 hours. Figure. 5 and 6 show the changes of intensity ratio and fluorescence

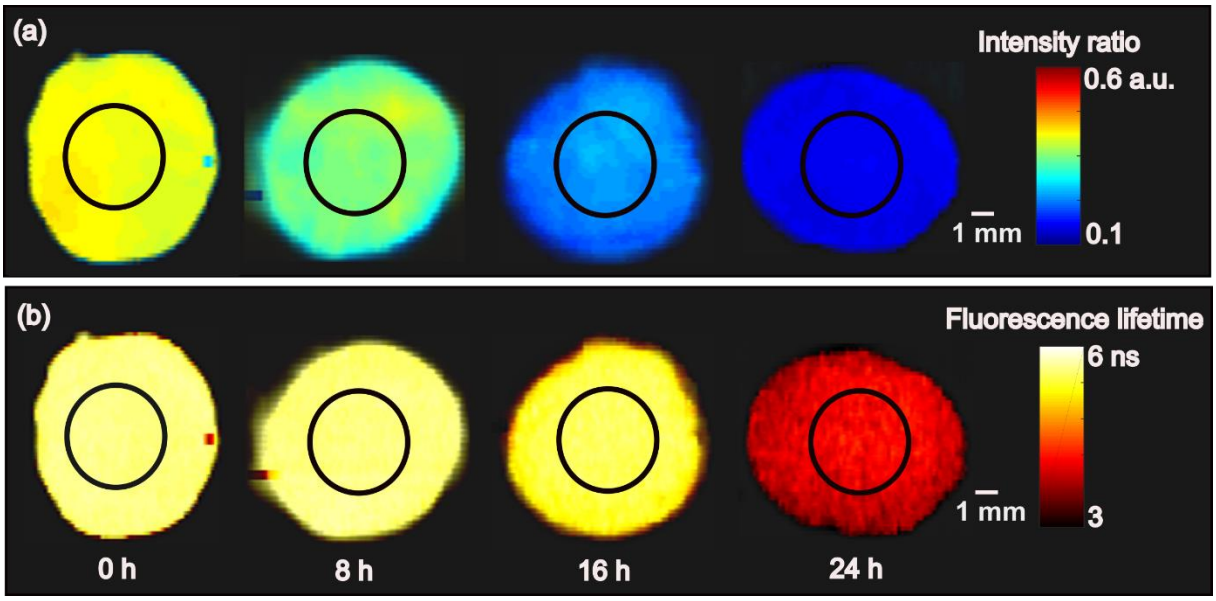

Figure 4. FLIm maps of digested BP. (a) Intensity ratio and (b) fluorescence lifetime maps of the digested group at 0, 8, 16 and 24 h time points. The black circle represents the region of interest within which data were analyzed.

lifetime, respectively. Kruskal Wallis H test results show a statistically significant difference between the digested groups over different exposure times ($p < 0.05$), but no difference for the control groups ($p > 0.05$). The Mann Whitney U test shows that Channel 1 (390/18 nm) and Channel 2 (435/40 nm) intensity ratios of the digested group are statistically different from those of the control group after collagenase degradation ($p < 0.05$; Fig. 5a and Fig. 5b). Channel 1 intensity ratio decreased 0.26 ± 0.02 after 24 hours, indicating that the fluorescence spectra of BP red shifted after collagenase degradation. This spectral red shift is quantitatively demonstrated by the change of intensity ratio using unstandardized mean difference between the control and digested groups, which shows a clear increasing trend in absolute values with digestion exposure time (Fig. 5a and 5b). The trend of change agrees with the hydroxyproline assay results (Fig. 3c), where the collagen content difference between 16 and 24 hours is smaller than that between 8 and 16 hours.

The same statistical analysis was performed for Channel 1 (390/18 nm) and Channel 2 (435/40

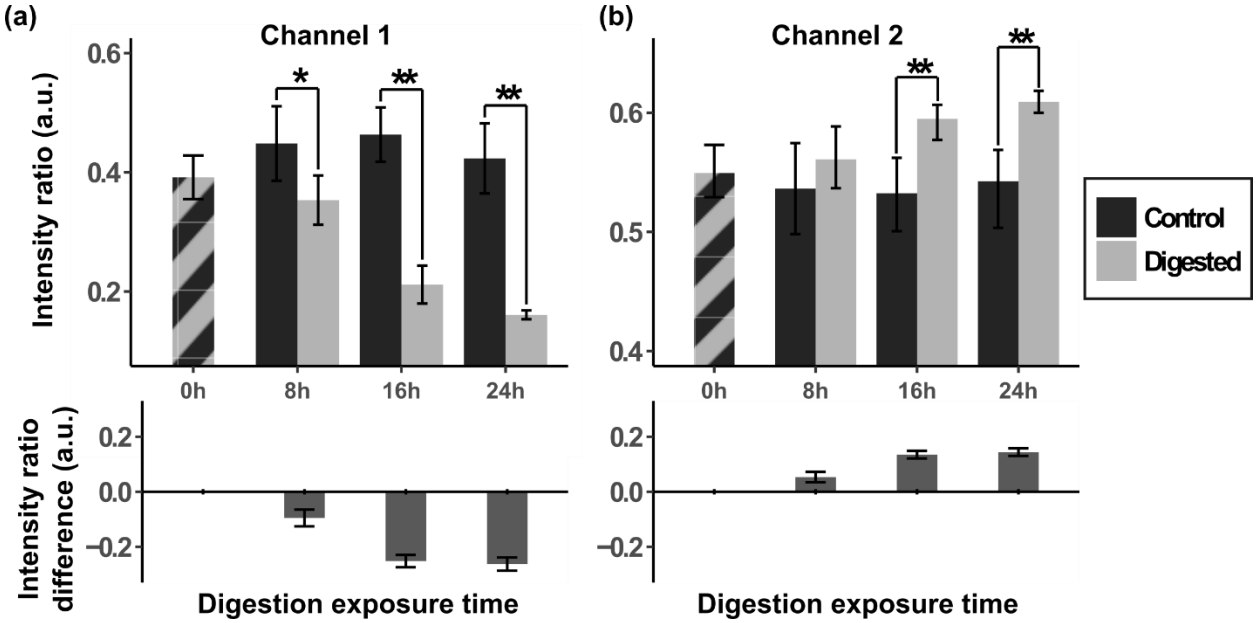

Figure 5. Changes of intensity ratio over different digestion exposure times. Columns represent two channels: (a) Channel 1 (390/18 nm) and (b) Channel 2 (435/40 nm). The figures in the above row show the intensity ratio change over different digestion exposure time in both channels. The figures in the bottom row show the unstandardized mean difference between the control group and digested group over different digestion exposure time in both channels. Hatch pattern represents that the digested group and control group are from same samples (*p<0.05; **p<0.01)

nm) fluorescence lifetime (Fig. 6). A decrease of fluorescence lifetime is observed for both Channel 1 and Channel 2 for later time points of collagenase digestion. However, the decrease of fluorescence lifetime was not significant at early stages of collagenase digestion before 16 hours time point. For Channel 1, there were significant decreases of 0.36 ± 0.10 ns on average after 16 hours digestion, and 1.37 ± 0.12 ns on average after 24 hours (Fig. 6a). For Channel 2, there was no significant change till the last time point where there was an average of 1.07 ± 0.13 ns decrease (Fig. 6b).

2.2.3.3 Correlation analysis

Kendall τ_B correlation analysis shows that different metrics of FLIm data were correlated with the collagen content, Young' Modulus and UTS (Figs. 7 and 8). Intensity ratios in Channel 1 (390/18 nm) and Channel 2 (435/40 nm) were significantly correlated with collagen content,

Young's Modulus and UTS ($p \leq 0.01$, Fig. 7). Fluorescence lifetime in Channel 1 correlated with the collagen content ($p < 0.01$, Fig. 8a), while the lifetime in Channel 2 did not ($p = 0.47$, Fig. 8d). Both of Channel 1 and Channel 2 lifetime showed correlations with Young's Modulus and UTS ($p < 0.01$, Fig. 8).

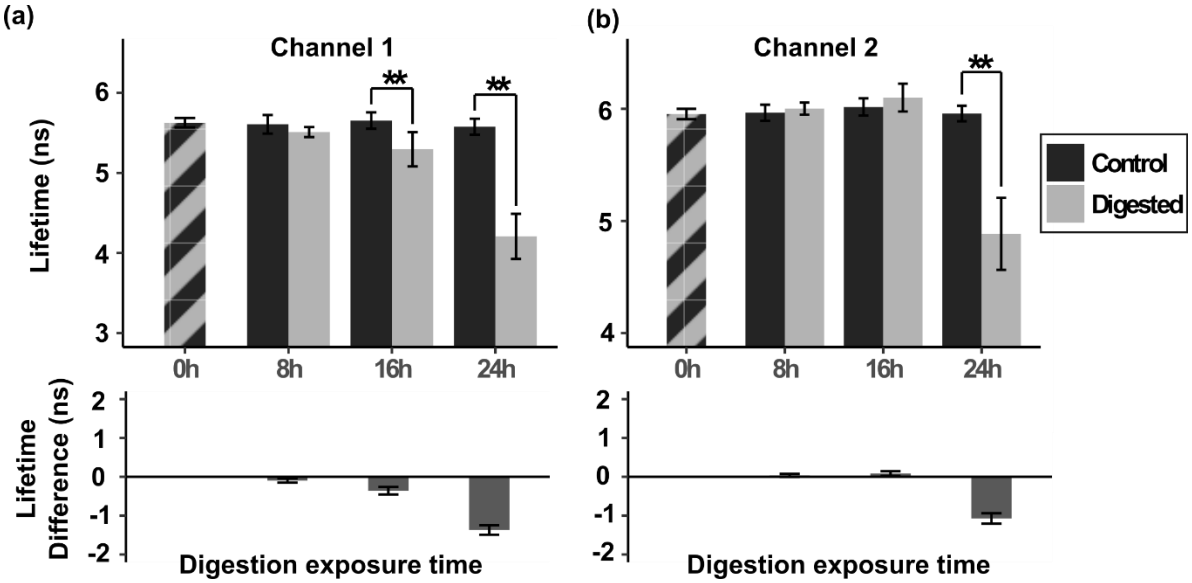

Figure 6 Changes of fluorescence lifetime over different digestion exposure times. Columns represent two channels: (a) Channel 1 (390/18 nm) and (b) Channel 2 (435/40 nm). The figures in the above row show the fluorescence lifetime change over different digestion exposure time in both channels. The figures in the bottom row show the unstandardized mean difference between the control group and digested group over different digestion exposure time in both channels. Hatch pattern represents that the digested group and control group are from same samples (*p<0.05; **p<0.01)

2.2.4 Discussion

Collagen is a dominant structural protein in most ECM [64]. Studies have shown that over 70% per dry weight (DW) of native BP is formed by collagen [65]. Following collagenase degradation, collagen is removed from BP matrix and the amount of extracted collagen was found related to the time that the matrix is exposed to collagenase, as shown in the results of collagen assay and histological images (Fig. 3). It is well known that collagen exhibits a fluorescence emission peak at 390 nm band upon UV excitation [66], [67]. The fluorescence

emission of our native BP was primarily detected in Channel 1 (390/18 nm) with a low signal detected in Channel 2 (435/40 nm). This suggests the possibility of using BP auto fluorescence to monitor the collagen loss during collagenase degradation. The observation, by a previous study [64], of a positive correlation between pericardium collagen content and elastic moduli motivated the use of a tensile testing in this study to measure the change in Young's Modulus and UTS as a function of collagenase digestion time. From Table. 1, it was found that the removal of collagen led to a decrease of Young's Modulus and UTS. The strong correlation observed between collagen content, Young's Modulus and UTS to FLIm measurement results, demonstrates the potential of the FLIm system for non-destructive assessment of the bio-chemical and bio-mechanical properties of BP during degradation processes.

Lewis et al. suggested measuring endogenous UV fluorescence intensity for probing the bio-mechanical properties of cartilage, however, it is known that the absolute intensity measurement is strongly dependent on the imaging configuration and prone to artefacts [58]. Therefore, in our study, the relative intensity ratio between different fluorescence emission bands and fluorescence lifetime are considered as better biomarkers for characterizing changes in BP during degradation. Intensity ratio is a measure of fluorescence emission spectrum and therefore related to matrix biochemical composition. The statistical analysis indicates that the collagen content, Youngs' Modulus and UTS are significantly correlated with the Channel 1 (390/18 nm) and Channel 2 (435/40 nm) intensity ratios (Fig. 7 and 8). In terms of fluorescence lifetime, the decreases in Channel 1 and Channel 2 lifetime agreed with the results of previous studies [60], [68]. Compared with intensity ratio, the correlation of lifetime with the conventional measurement results is marginally weaker. However, the lifetime measurement modality still has value because there are situations where only the

lifetime changes while the spectrum remains the same, as observed by Manning et al. in their cartilage degradation study [60].

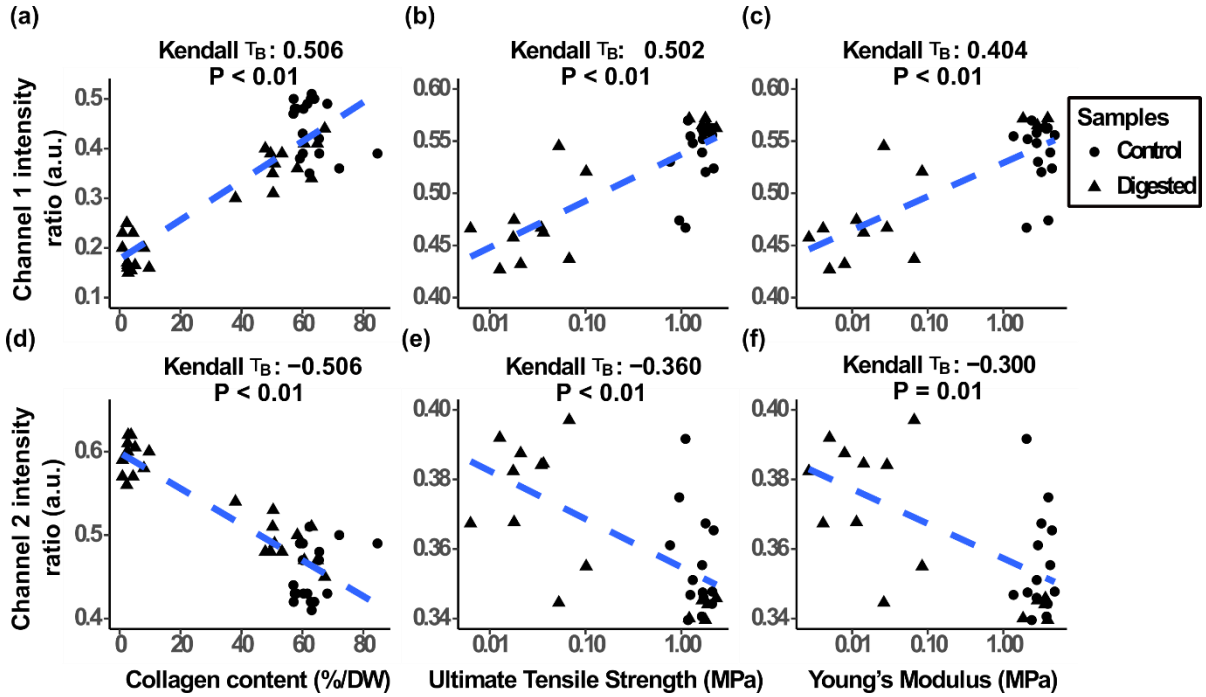

Figure 7. Correlations of (a) Collagen content vs. Channel 1 (390/18 nm) intensity ratio, Ultimate Tensile Strength (UTS) vs. Channel 1 intensity ratio, (c) Young's Modulus vs. Channel 1 intensity ratio and (d) Collagen content vs. Channel 2 (435/40 nm) intensity ratio, (e) UTS vs. Channel 2 intensity ratio, (f) Young's Modulus vs. Channel 2 intensity ratio. The Kendall τ_B and p value of each combination are shown in the plot. The trend was demonstrated by the blue dashed line for the variables that are significant correlated ($p \leq 0.01$).

2.2.5 Hypothesis about the cause of fluorescence spectrum and lifetime changes

2.2.5.1 Sample preparation

For explaining the observed changes of emission spectrum and lifetime, the effect of solvent was studied by measuring native and 16 hours digested BPs in solutions of different polarities. The solutions were made by mixing PBS with pure (100%) ethanol at different volume ratios. Since ethanol is less polar than water, increasing the solvent ethanol concentration decreases the polarity of the solvent. Four 16 hours digested samples (processed the same as described

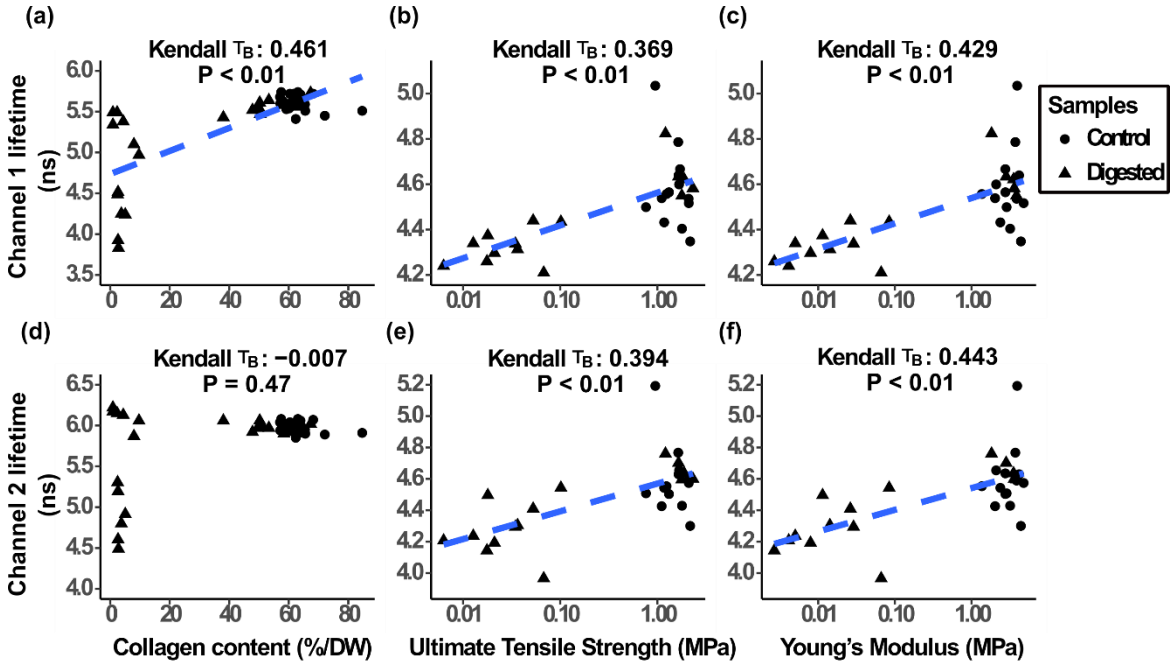

Figure 8. Correlations of (a) Collagen content vs. Channel 1 (390/18 nm) lifetime, (b) Ultimate Tensile Strength (UTS) vs. Channel 1 lifetime, (c) Young's Modulus vs. Channel 1 lifetime and (d) Collagen content vs. Channel 2 (435/40 nm) lifetime, (e) UTS vs. Channel 2 lifetime, (f) Young's Modulus vs. Channel 2 lifetime. The Kendall τ_B and p value of each combination are shown in the plot. The trend was demonstrated by the blue dashed line for the variables that are significant correlated ($p \leq 0.01$).

above) were measured by FLIm in the pure PBS, 30% ethanol, 60% ethanol and pure ethanol, while the remaining two native BP samples were measured in pure PBS and pure ethanol for comparison. The measurements were taken immediately after samples were immersed in ethanol solutions to avoid collagen structure being changed.

2.2.5.2 Results

The effect of solvent polarity on fluorescence lifetime and intensity ratio is shown in Fig. 9. The polarity of solvent increases when ethanol is mixed with PBS in less concentration. As shown in Fig. 9a and 9b, for 16 hours digested BP, with increasing solvent polarity, Channel 1 (390/18 nm) intensity ratio decreased, and Channel 2 (435/40 nm) intensity ratio increased. This is consistent with the red shift we observed after collagenase degradation (Fig. 5). For native BP, a red shift also occurred for samples measured in ethanol, but the observed change

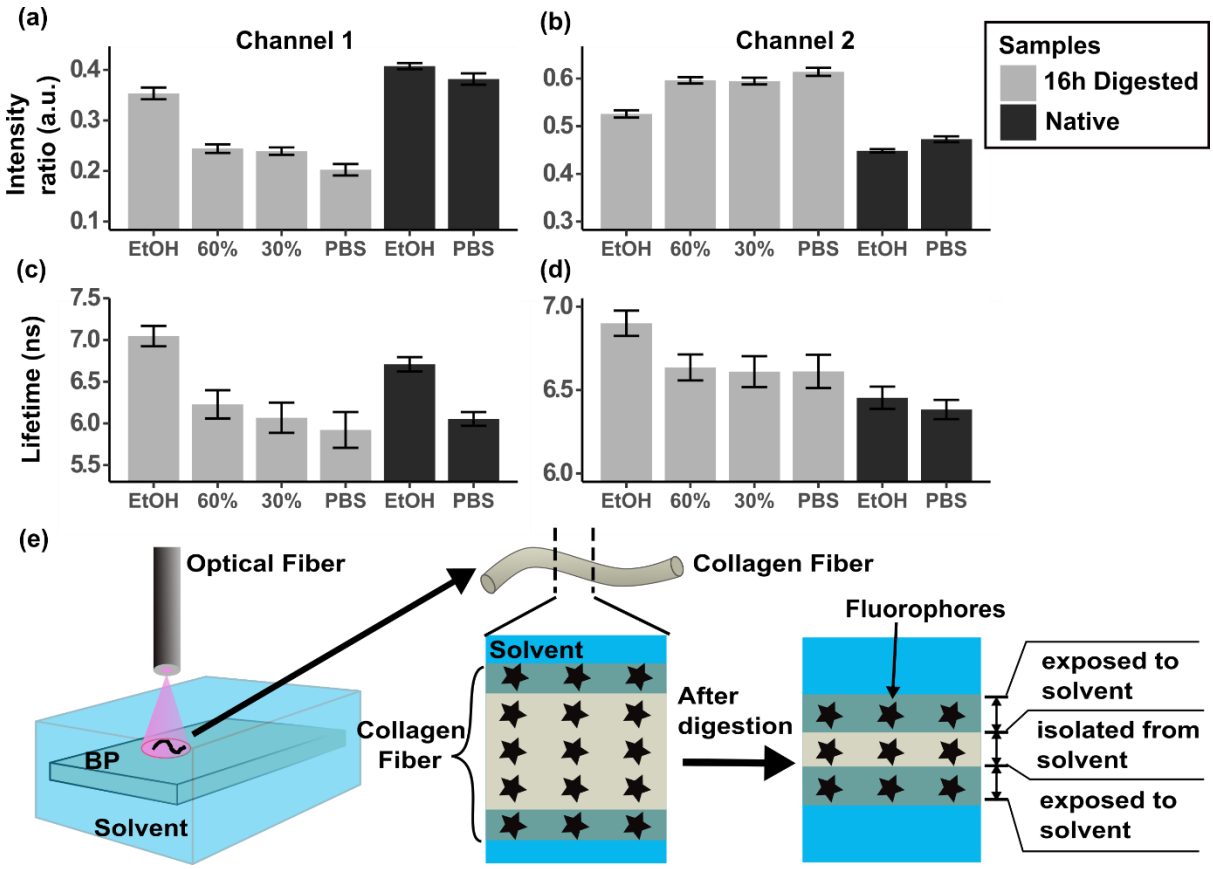

Figure 9. Lifetime and intensity ratio changes due to the solvent effect. (a) Channel 1 (390/18 nm) and (b) Channel 2 (435/40 nm) intensity ratio of the native BP and 16 h digested BP in different solvents; (c) Channel 1 and (d) Channel 2 lifetime of the native BP and 16 h digested BP in different solvents. EtOH represents pure ethanol, X% represent X% of solution is ethanol. PBS represents pure PBS solution. (e) Schematic of the solvent effect hypothesis for explaining the change observed on fluorescence spectra and lifetime. The measured BP fluorescence signal has to main contributions: (1) fluorophores on the surface whose signal is affected by the surrounding solvent; (2) fluorophores isolated from the solvent whose signal will not be affected by it. After collagenase degradation, the structural changes on the collagen fibers result in relatively more fluorophores get exposed to solvent and are affected by the solvent effect.

was much smaller than for the 16 hours digested BP. Similarly, fluorescence lifetime was affected by the solvent polarity. With increasing solvent polarity, Channel 1 and Channel 2 fluorescence lifetime of both digested and native BP decreased. Note that the intensity ratios of native BP in PBS are closer to those of digested BP in ethanol, while the lifetimes of native BP in PBS are close to those of digested BP in PBS, which indicates that the lifetime is more sensitive to the solvent effect than intensity ratio.

2.2.5.3 Discussion

As discussed above, the collagenase degradation caused the emission spectrum to red shift and the lifetime to decrease. One possible explanation is that the collagenase degradation caused a change of relative amounts of different fluorophores, for example, the ratio of pentosidine to pyridinoline, both of which are known crosslinking elements present in collagen matrices and will fluoresce upon UV excitation [58]. However, the bacterial collagenase I used is known to be highly active for digesting collagen by directly attacking the triple helical regions [69]. For BP, a biomaterial dominated by collagen [65], the effect of collagenase degradation is more likely to be a removal of whole collagen fibrils rather than specific components. Therefore, it is not likely that the observed spectral and lifetime changes were due to the relative changes of different fluorophores. A plausible explanation was proposed by Manning et al. who postulated that the decrease of lifetime resulted from the micro-environment changes of collagen crosslink sites within the fibrils during collagenase degradation [60]. In this paper, we expand on this hypothesis by investigating the impact of solvent polarity on fluorescence emission. We found a spectral red shift and a lifetime decrease when the sample was exposed to solvent with higher polarity (Fig 9a - d). Both changes due to the solvent effect have been previously well studied [70]. For this study, we consider some of the fluorophores in a collagen fiber (represented by stars in Fig. 9e) to be located closer to the surface while the rest are inside the fiber, isolated from the solvent. Since all measurements were performed with the samples surrounded by PBS, the surface fluorophores were exposed to an aqueous high polar solvent, such as water, causing the emission spectrum to red shift and fluorescence lifetime to decrease. After collagenase degradation, the shrinkage of collagen fibers caused by the removal of collagen, gave rise to

an increase ratio between fluorophores exposed to solvent and fluorophores isolated from solvent, magnifying the spectral red shift and the decrease of fluorescence lifetime.

2.3 Conclusion

In conclusion, the collagen content, Young's Modulus and UTS of native bovine pericardium have been shown to strongly correlate with the relative intensity ratio between different fluorescence emission bands, and significantly correlate with fluorescence lifetime. Thus, FLIm is capable of non-destructively monitoring biochemical and biomechanical changes of BP during collagenase degradation. A model for predicting collagen content and the biomaterial's mechanical properties using FLIm metrics, such as intensity ratio and fluorescence lifetime, would be of great value for the tissue engineering community, as it could potentially replace conventional approaches by non-destructive, less costly, and faster measurements, enabling *in situ* monitoring of engineered biomaterials properties for TEVG development.

Chapter 3: Optical imaging system for non-destructive monitoring of vascular graft maturation in bioreactor

3.1 Introduction

3.1.1 Bioreactor and its applications

Chapter one described that an ideal TEVG should possess appropriate mechanical properties (burst pressure, compliance, elasticity), biological functions (ECM composition, cellularity) and structure (lumen diameter, structural integrity). The TEVGs made from scaffold-based methods, decellularized matrix based methods or self-assembly method, may not present all these properties after the tubular constructs are initially shaped. To mature the TEVG before implantation, *in vitro* culturing vascular graft inside the bioreactor using growth factors and mechanical stimulation is preferred [71]. Bioreactors are defined as devices in which biological and/or biochemical processes develop under closely monitored and tightly controlled environment (e.g., pH, temperature, pressure, nutrient supply and waste removal) [72]. The capability of accurately controlling the culturing condition have been shown advantageous to vascular graft maturation. For example, carefully modulating the growth factor can improve the phenotype of cells and mechanical stimulation by modulating the flow condition can increase the tissue mechanical strength [73], [74]. It is also possible to completely automate the culturing of TEVG using the bioreactor, which is important for transferring to large-scale applications [72]. When designing bioreactors, researchers will take both biochemical and biomechanical control into consideration. For the bioreactor used for TEVG culturing, this control is usually realized by generating the fluid flow passing through the vascular graft, that has the desired composition, flow rate, pressure and temperature [75]. A bioreactor used for TEVG includes three basic components: 1) a flow cell where the TEVG is mounted and immersed by the media; 2) a pump that generates the flow circulating through

the whole bioreactor system; 3) a reservoir that can exchange media/air/mass to maintain the nutrition of media [76]. Many bioreactors have been proposed and tested for TEVG development while challenges remain like 1) a need to adapt the culture conditions to the maturation of vascular graft based on the feedback about its properties; 2) the lack of knowledge for the growth and remodeling of TEVG during culturing; 3) the barrier in terms of cost and time spent on this kind of studies. In this chapter, we explored how the optical imaging technique can help solve these challenges. This chapter is modified from our previous work [77], with the approval from *Methods and Applications in Fluorescence* ().

3.1.2 Imaging inside the bioreactor

Previous chapters have examined the imaging techniques used for characterizing tissue properties. At that stage, the samples are of regular shape and can be measured by benchtop systems. After shaping to the tubular structure and culturing inside the bioreactor, cross-sectional imaging or intraluminal imaging become necessary. Non-destructive evaluation of TEVG morphology has previously been implemented with magnetic resonance imaging (MRI) by Mertens et al. [78]. For that work, ultrasmall superparamagnetic iron oxide (USPIO) nanoparticles were incorporated into the polymer matrix and further cultured in the bioreactor. In addition, Whited et al. utilized fluorescence imaging for tracking endothelization of the luminal side of TEVG cultured inside a bioreactor. Their strategy consisted of embedding two micro capillary channels for fiber optic excitation of the GFP-labeled endothelial cells [47]. Despite the success of these methods to accomplish longitudinal monitoring of tissue development, TEVGs were heavily modified for imaging purposes, increasing their complexity in detriment of their potential for further development [79]. Label-free imaging

techniques can circumvent some of these pitfalls and reduce the complexity of sample preparation. For example, the potential of intravascular optical coherence tomography (OCT) for imaging TEVGs inside bioreactors was reported with remarkable results in resolving wall thickness and scaffold degradation [80]. Moreover, a recently developed micro-OCT (μOCT) technique has shown potential to image the endothelial cell layer in coronary arteries [81]. While OCT excels at resolving these structural features in tissues, it fails to provide functional information associated with bio-chemical changes of the TEVGs.

3.1.3 Endogenous and exogenous fluorescence imaging system

Endogenous fluorescence, as discussed in chapter two, reports on biochemical and biomechanical features of tissue samples. A previous study from our group also demonstrated the possibility of resolving seeded cells from a collagenous matrix measuring endogenous fluorescence lifetime [82]. However, for all these studies, the imaging conditions were favorable: the flat sample geometry enables a tight control of the probe-to-sample distance and validation of cell presence was easily performed by conventional fluorescence microscopy. But imaging inside a bioreactor complicates the geometry of the sample and the probe-to-sample distance becomes more difficult to control. In this chapter, we utilized the flexibility of fiber-based imaging and validated the system ability for imaging luminal cell presence in the bioreactor. We also incorporated an intensity-based exogenous fluorescence imaging system to the FLIm instrument that acquires specific fluorescence from cell markers in parallel and co-registered to the endogenous fluorescence lifetime images.

In the rest of chapter, a fiber based dual-modality instrument is described that combines a multi-spectral fluorescence lifetime imaging (FLIm) module that allows for measurements of tissue autofluorescence with a steady-state module tailored to imaging of cells expressing

enhanced green fluorescence protein (eGFP) [29]. The system is then adapted to intraluminal imaging in a bioreactor and its sensitivity for cellular fluorescence was demonstrated. Here we described the integration of the dual-modality system with a custom-built bioreactor for TEVGs growing by adapting a fiberoptic probe for side-viewing illumination/collection and intraluminal imaging via reciprocal scanning. The instrument accuracy to time-resolved fluorescence was demonstrated by measuring fluorescent dyes with distinct lifetime. The spatial resolution of the fiberoptic scanning probe was estimated by imaging a stent phantom. Finally, the sensitivity of the integrated instrument was evaluated by imaging tissue samples in the bioreactor and resolving human mesenchymal stem cells fluorescence from antigen-removed bovine pericardium tissue matrix. This system could be easily adapted for other reported TEVG bioreactors given the flexibility of the optical fiber probe [83], [84].

3.2 The endogenous and exogenous fluorescence imaging system used for imaging vascular graft inside the bioreactor

3.2.1 Bioreactor assembly

A custom bioreactor was designed and fabricated. Figure. 10 depicts the bioreactor composed of a custom-made graft chamber, a media reservoir, and a pulsatile pump. Figure. 10a shows a schematic of the bioreactor with a rendering of the graft chamber. The chamber consisted of two pairs of 3D printed polysulfone flanges (Protolabs, USA) connected by two blunt-tip stainless steel dispensing needles (6710A41, McMaster-Carr, USA) with distal end sealed by heat curing epoxy (353 ND-T, Epoxy Technology, Inc. USA). The inner and outer parts of the polysulfone flanges were attached with two sets of stainless-steel socket cap screws and sealed inside an O.D. 25 mm Pyrex glass tube by two 1.5 mm wide, I.D. 17 mm chemical resistance O- rings (1185N39, McMaster-Carr, USA). Stainless steel straight connectors (SBP-140-SS, Pneumadyne, Inc. USA) were used to hold the vascular grafts inside the

chamber. All the connectors and dispensing needles were further sealed with chemical resistance O-rings (McMaster-Carr, USA). The flow circuit included a media reservoir consisting of a 100 mL Pyrex media bottle. The cap of the bottle was laser cut and replaced with a thin polydimethylsiloxane (PDMS) cap that allows for gas exchange to maintain adequate oxygen, CO_2, and humidity levels inside the bioreactor. Barbed connectors and silicon tubing were used to circulate media between the reservoir and the graft chamber. The pulsatile flow was generated by attaching the silicon tubing to a 4-channel peristaltic pump (FH100M, Thermo Scientific, USA) that pumps the media from reservoir to the graft chamber. A Y connector was used to split the flow: one went through the intraluminal surface of the vascular graft while the other entered the chamber through the dispensing needles and circulated outside the graft (Fig. 10b). The two flows were combined by another Y connector

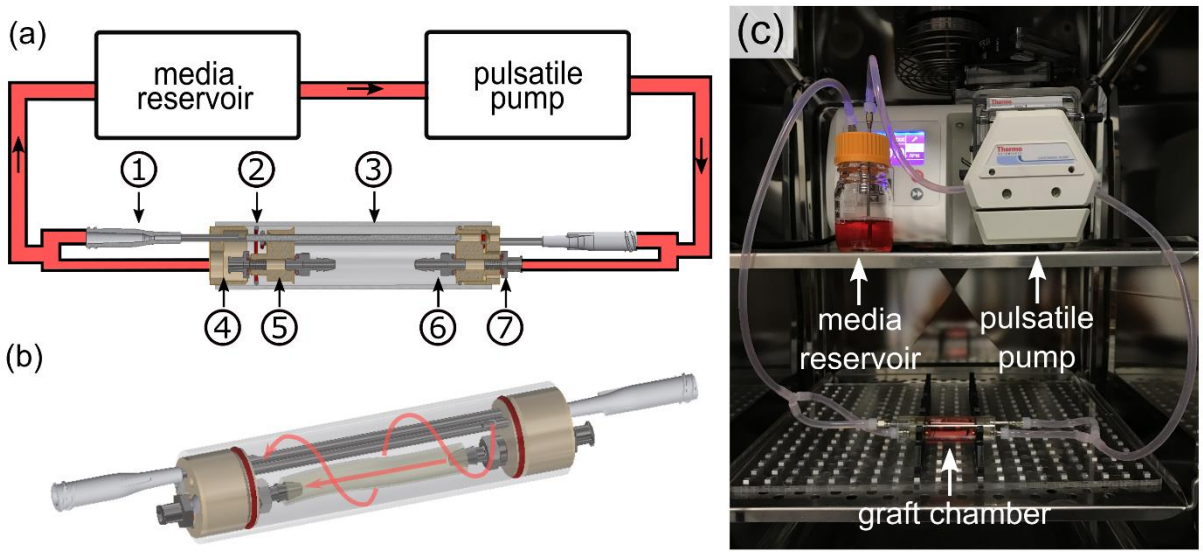

Figure 10. Bioreactor. (a) Schematic of the bioreactor with a media reservoir, the pulsatile pump and a custom graft chamber. The flow circulation direction is represented by the arrows in the tubes (in red). The graft chamber is composed of: ① stainless-steel dispensing needle with distal end sealed by heat-curing epoxy, ② chemical-resistant O-ring, ③ Pyrex glass tubing, ④ polysulfone inner flanges, ⑤ polysulfone outer flanges, ⑥ stainless-steel straight connectors, ⑦ stainless-steel female luer. (b) Schematic of flow circulation inside the assembled graft chamber. One flow went through the intraluminal surface inside graft and the other circulates outside the graft. (c) Photograph of the bioreactor inside the incubator.

and guided back to the media reservoir, completing the circuit. The entire setup was placed inside an incubator at 5% CO_2 and 37.0˚C (Fig. 10b). All the parts of the graft chamber, the reservoir, and the tubing were autoclaved prior to any use.

3.2.2 Imaging system design

3.2.2.1 FLIm modality

Figure. 11a shows a schematic of the dual-modality endogenous and exogenous (eGFP) fluorescence system that was included in our recent work [29]. Briefly, the FLIm module allowing for measurements of tissue endogenous fluorescence consisted of a 355 nm excitation pulsed laser generated by third harmonic generation of a passive Q-switched Ni:YAG laser (STV-02E, TEEM photonics, France). The emitted fluorescence was collected

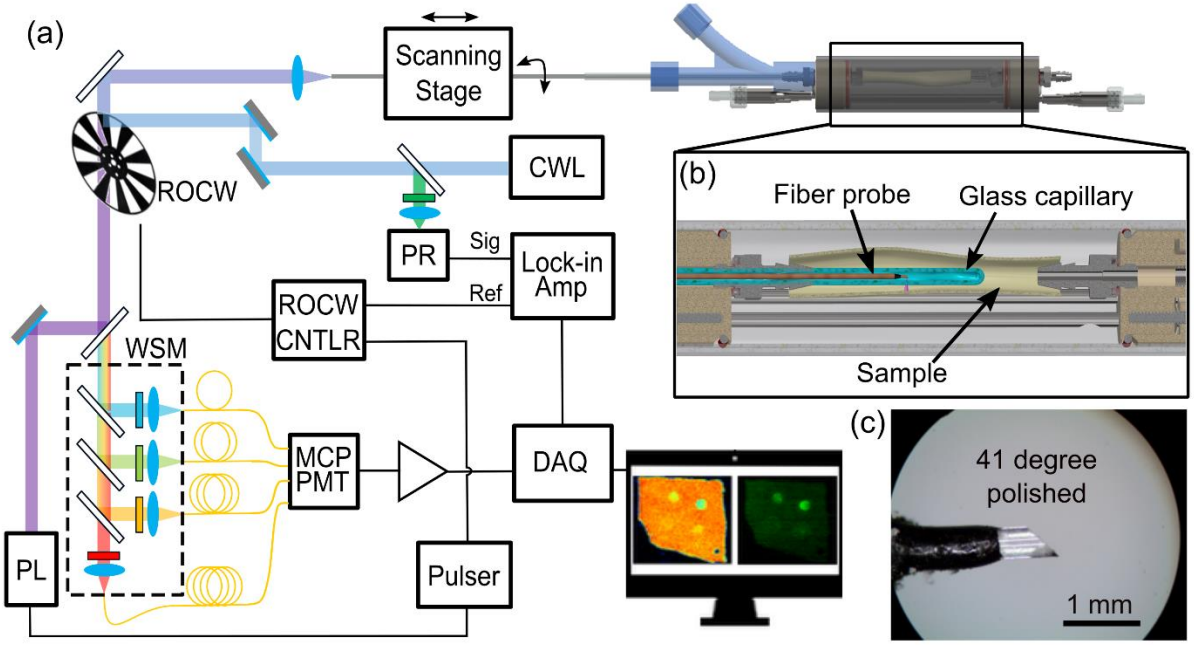

Figure 11. Imaging setup. (a) Schematic of the endogenous and exogenous fluorescence system applied to luminal scanning inside the bioreactor graft chamber. PL: 355 nm pulsed laser; MCP PMT: microchannel plate photomultiplier tube; WSM: wavelength selection module; ROCW: reflective optical chopper wheel; DAQ: digitizer; PR: photoreceiver; CWL: 440 nm continuous-wave laser. (b) The cross section view of the graft chamber showing the side viewing fiber probe and the glass capillary used as imaging channel. (c) Microscope photograph showing the angle polished Bessel probe.

by a wavelength selection module (WSM) to four different spectral bands (spectral bands: SB1: 381 - 399 nm, SB2: 415 - 440 nm, SB3: 532 - 553 nm, SB4: 572 - 642 nm). After the WSM, four delay fibers of different length (1, 10, 19 and 28 m) sent light from each spectral band sequentially into a single microchannel plate photomultiplier tube (MCP PMT, R3809U-50, Hamamatsu, Japan) and the electronic signals were further amplified and sampled by a high-speed digitizer running at the sampling rate of 12.5 GS/s (NI PXIe-5185, National Instruments, USA).

3.2.2.2 Incorporation of steady-stage intensity fluorescence modality

Because the excitation pulse of the FLIm module was generated at 1 kHz and the fluorescence signal always decays in the order of 1-10 ns, the duty circle of this module is less than 0.1%. This generates a big silent time window, creating an opportunity to interleave other imaging modalities in the system, for example, a module for detection of exogenous probes fluorescence emission. A 10-slot reflective optical chopper wheel (ROCW, MC1F10A, Thorlabs, Inc. USA, shown in Fig. 12) was placed in the optical path and synchronized with

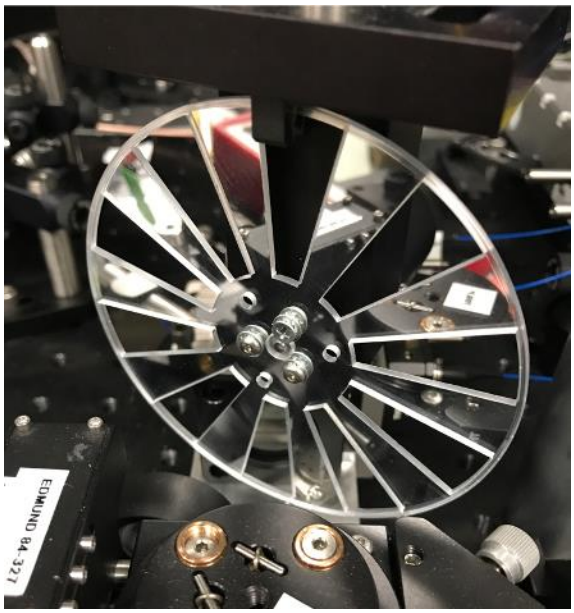

Figure 12. Reflective optical chopper wheel with 10 slots

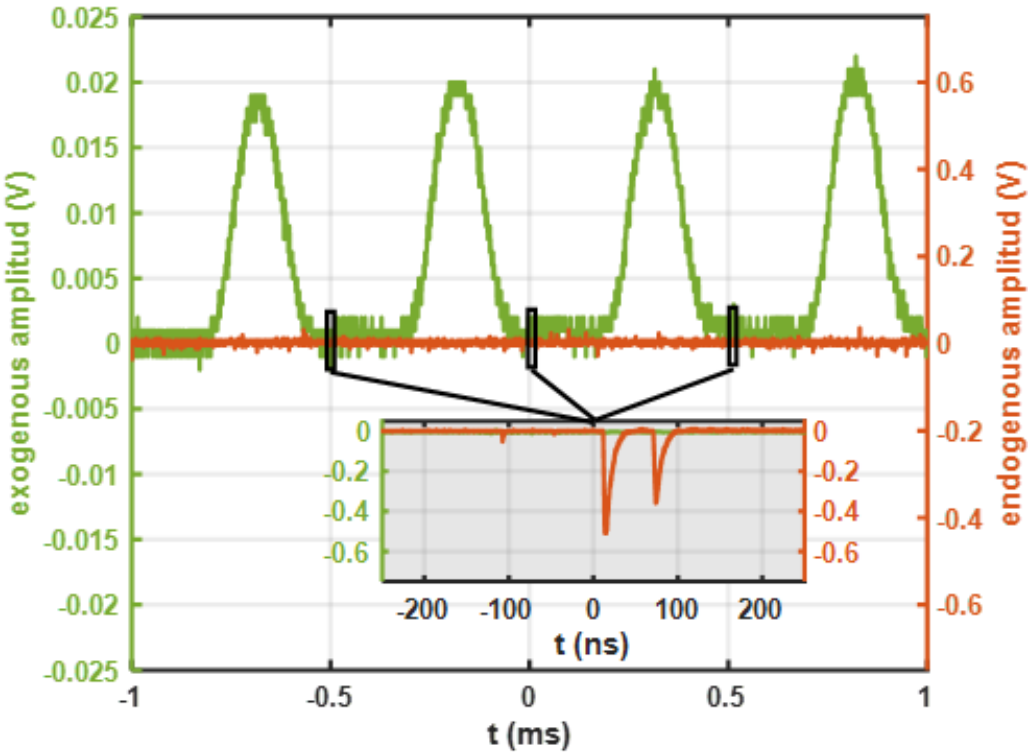

Figure 13. Recorded raw signal of FLIm and exogenous cw fluorescence (eGFP) system. The fluorescence signal was generated by placing a chroma slide in front of the imaging probe. Green color represents exogenous fluorescence (eGFP) signal while the red color represents the FLIm signal

the FLIm excitation (UV pulsed laser) such that it transmits the UV pulses and the endogenous fluorescence for FLIm, and it reflected the exogenous excitation and emission to the steady-state fluorescence imaging system. The eGFP fluorescence was induced by a continuous wave (cw) laser centered at 440 nm (TECBL-50G-440-USB, World Star Tech, Canada) and detected by a photoreceiver (2001-FS, Newport, USA) with a band pass filter (510/84 nm) in front. In this way, the eGFP fluorescence and endogenous FLIm data are co-registered and synchronously measured. As shown in Fig. 13, the endogenous signal (FLIm) and exogenous signal (eGFP) are interleaved and there is no crosstalk between each other. We further increased the sensitivity of our instrument by extracting the exogenous emission signal at the carrier frequency of 1 kHz from the photoreceiver output with a lock-in amplifier (SR530, Stanford Research Systems, USA), using the output from the ROCW controller (MC1000,

Thorlabs, Inc. USA) as reference. The magnitude output of the lock-in amplifier was then sampled by another digitizer (NI PXIe-5114, National Instruments, USA) running at the sampling rate of 20 kS/s.

3.2.2.3 Helical scanning

To image the luminal surface of vascular grafts inside the bioreactor, a 2 mm I.D. and 3 mm O.D. borosilicate glass tube with one end sealed was inserted all through the graft chamber providing a transparent imaging channel (Fig. 11b). A side-viewing optical fiber probe was then inserted into the glass tube for imaging. The scanning was performed by reciprocally rotating the optical fiber probe with a NEMA 8 hollow shaft stepper motor (8HY0001-7SK, Jinan Link, China) and pull-backed by a uniaxial stage (Parker, USA). Figure. 11c shows the distal end of the side viewing optical fiber probe, a 400 μm multimode fiber (FVP400440480, Polymicro Technologies, USA) polished at 41° (the angle between the fiber axis and the polishing surface) and glued to a 19 Gauge hypodermic tube by heat curing epoxy (320, Epoxy Technology, Inc. USA).

3.2.3 Phantom measurement

The dye phantom was made from four small quartz capillaries with different fluorescent dyes inside and attached around the borosilicate glass tube that was used for imaging in the bioreactor (Fig. 14a). The four dyes included two fluorescent dyes: 5 mM Fluorescein and 100 μM Rhodamine 6G, both dissolved in ethanol, as well as two tissue endogenous fluorophores: 500 μM NADH (Sigma, USA) on 0.1 M MOPS buffer (Alfa Aesar, USA), and 2 mg/ml FAD (Sigma, USA) in pure water. The dye solutions were injected into small capillaries sealed on both ends and fixed around the borosilicate glass tube. During imaging, a 2 cm section was imaged with the system by inserting the optical fiber probe through the

glass imaging tube. Scanning was performed with a step-size of 2° in the circumferential direction and 200 µm in the axial direction.

The second phantom was made of fluorescent Polymethylmethacrylate (PMMA) with a drug-eluting stent (wire diameter of around 40 µm; AXUS Libert´e Atom Paclitaxel Eluting Coronary Stent System, Boston Scientific, USA) placed inside to provide structural features, and it was used for estimating the resolution of the imaging system (Fig. 14b). The borosilicate glass tube was inserted inside the phantom to image the stent with 2° and 200 µm step size.

The two custom phantoms used for the evaluation of dual-modality system performance are depicted in Fig. 14a and 14b. Figure. 14c shows the intensity weighted fluorescence lifetime

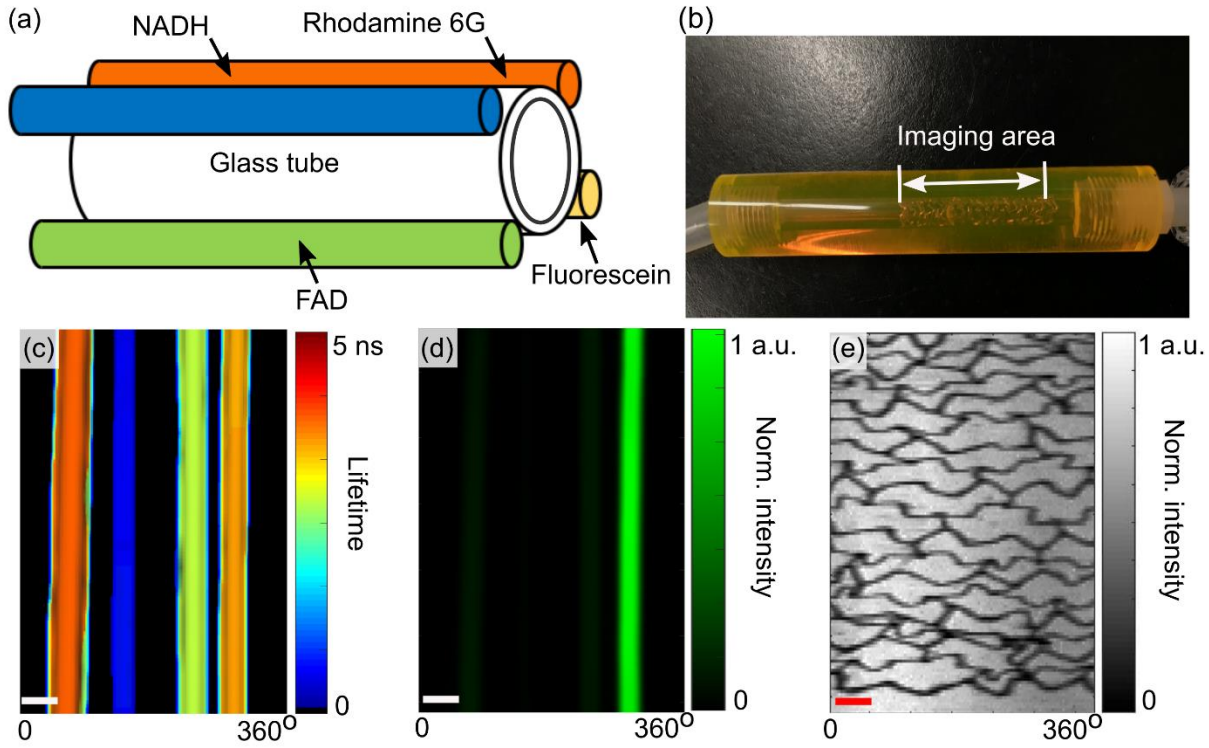

Figure 14. Phantom imaging. (a) Schematic of the phantom. Four glass capillaries filled with Rhodamine 6G, NADH, FAD and Fluorescein were attached to the borosilicate tube, used as imaging channel. (b) Photograph of the stent phantom. (c) Intensity weighted lifetime image at SB3 (532 - 553 nm) of dye phantom. From left to right, the four columns represent Rhodamine 6G, NADH, FAD and Fluorescein. (d) Normalized eGFP fluorescence intensity image of dye phantom. Only fluorescein was visualized (e) normalized intensity image of the stent phantom at SB3. All three scale bars in (c-e) represent 2 mm.

images in SB3 (532-553 nm) which exhibits fluorescence from all chosen fluorophores. The mean ± standard deviation fluorescence lifetime in SB3 were calculated to be: 0.61 ± 0.06 ns for NADH, 2.72 ± 0.06 ns for FAD, 3.82 ± 0.04 ns for Rhodamine 6G and 3.49 ± 0.09 ns for Fluorescein, consistent with literature values [85]–[87]. Figure. 14d shows the normalized eGFP fluorescence intensity image acquired within the same measurement, where fluorescein was visualized easily. Fig 14e shows the SB3 normalized intensity image of the stent phantom in gray scale. The fluorescence originates from the main body of the stent phantom made of PMMA with a strong fluorescence in SB3 that serves as background for visualizing the stent itself. From the image, it is easy to resolve the fine structure of the stent (in black) that has an average diameter of 40 µm measured under the microscope.

3.2.4 Biological sample measurement

To demonstrate the system's potential for imaging in bioreactor-based applications, We tested the system's ability to detect human mesenchymal stem cells (hMSC) seeded on the luminal serous surface of antigen removed bovine pericardium (AR-BP) prepared as previously described [12], [88]. Fig 15a shows the procedure of tissue sample preparation. AR-BP was locally seeded with eGFP-hMSC as detailed elsewhere [82]. Six AR-BP pieces of 1.5 cm wide by 4 cm long were washed in cell culture media consisted of DMEM high glucose, 1% (vol/vol) penicillin-streptomycin, 1%(vol/vol) L-glutamine 200 mM (Hyclone Laboratories, South Logan, UT, USA), and 20% (vol/vol) FBS (Atlanta Biologicals, Lawrenceville, GA, USA) overnight on a shaker at 4°C. 70 µL with 40,000 eGFP-hMSC were seeded using a glass cylinder (Pyrex cloning cylinder, inner diameter 4 mm) onto the serous side of AR-BP. After overnight incubation, the cylinders where removed and cell attachment was confirmed by fluorescence microscopy (eGFP filter set Ex 470/40 nm, Em 525/50 nm, Dichroic mirror at

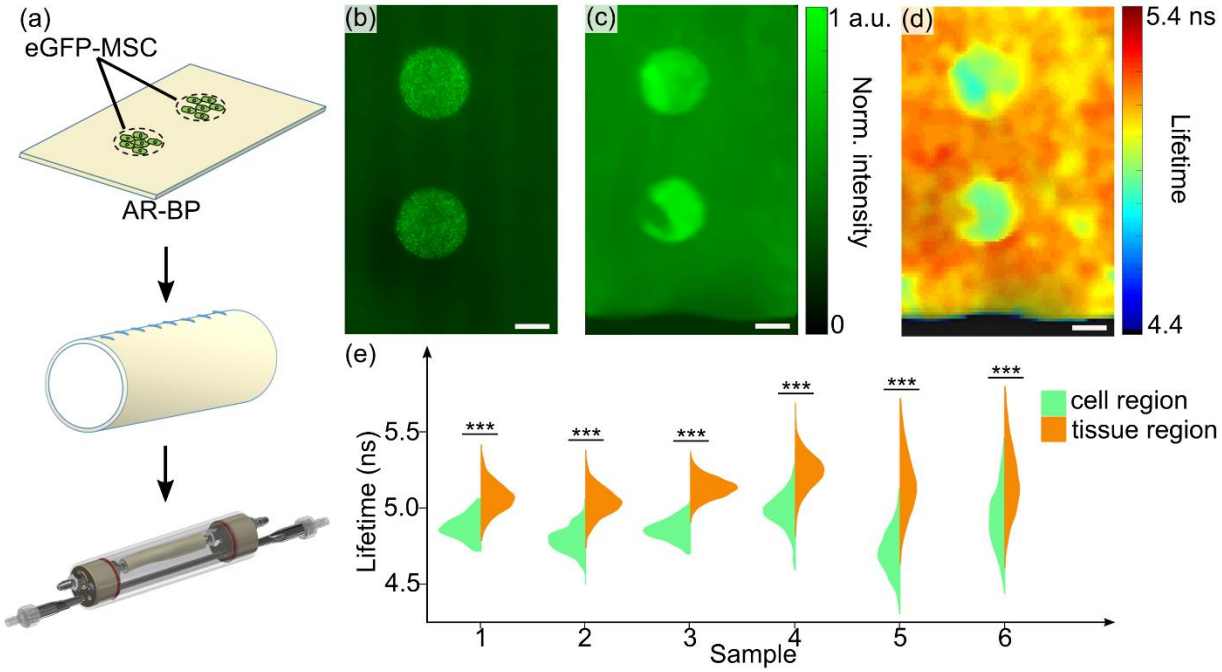

Figure 15. Images of eGFP-hMSC seeded antigen removed bovine pericardium representative sample. (a) Schematic of sample preparation. (b) Fluorescence microscopy image of the flat sample before suturing. (c) Normalized eGFP fluorescence intensity intraluminal image of the same sample inside the bioreactor. (d) Corresponding intensity weighted fluorescence lifetime intraluminal image at SB3 (532 - 553 nm). (e) Split violin plot of SB3 lifetime distributions between cell and tissue regions for all six samples. The stars represent the statistical significance calculated with Student's t-test (*** $p<0.001$). All scale bars represent 2 mm.

495 nm: BZ-X710, Keyence Itasca, IL, USA). Full scaffold images were taken with a Plan Fluor 4x/0.13NA objective lens (Nikon, Japan). The scaffolds were subsequently sutured with a simple continuous 6-0 proline suture joining the two 4 cm long sides to one another to form a tubular shape and onto the bioreactor graft chambers for imaging. The imaging was performed by inserting the glass tube first and then the side viewing fiber probe which was moved with a step size of 5° in the circumferential direction and 200 µm in the axial direction. All the endogenous fluorescence lifetime images and exogenous eGFP fluorescence intensity images were denoised using box filters for better display. The statistical analysis of lifetime difference between cell and tissue regions was performed comparing pixels within these two

regions of the lifetime images for all six samples. A split violin plot was used to display the lifetime distribution of these two regions and a Student's t-test was used to testify their significant difference. The processing was performed in MATLAB 2018a and RStudio.

Fig 15b shows the eGFP fluorescence intensity image of a representative flat hMSC seeded AR-BP before suturing, acquired by conventional fluorescence microscopy. Cells are localized in two circular regions. Figure.15c shows the eGFP exogenous fluorescence image of the luminal surface same sample sutured on the bioreactor acquired using the dual modality fiberoptic system. The two circular cellularized regions were successfully detected. The image also shows that part of the bottom cellularized area was compromised likely during sample preparation. Fig 15d shows the corresponding SB3 (532 - 553 nm) endogenous fluorescence lifetime image of sample, which was acquired in parallel with Fig. 15c. There is a clear contrast between the cell seeded region with a lifetime of 4.88 ± 0.08 ns and the non-cell seeded region with a lifetime of 5.14 ± 0.09 ns. The split violin plot (Fig. 15e) shows the SB3 lifetime distributions of cell and tissue regions for all six samples, which all followed an equivalent trend. The fluorescence lifetime of cellularized areas decreases an average of 0.33 ± 0.21 ns with respect to the acellular scaffold ($p<0.001$). The variance is attributed intrinsic sample variations. The trend of lower lifetime for cell seeded region was found consistent with previous studies [82].

3.2.5 The steady-state system optimized for other dyes

The ROCW has high reflectance over a broad spectral bandwidth so the system is flexible for imaging other exogenous dyes. To demonstrate the system's flexibility, we tailored the exogenous fluorescence imaging modality to another red fluorescent protein (dsRed). On the AR-BP, we seeded the dsRed-labeled and un-labeled cells locally using the cylinders. After

overnight incubation, the cylinders were removed, and the sample was imaged by fluorescence microscope to validate cellular presence. The sample was then scanned by our dual-modal system.

Figure. 16a shows the dsRed fluorescence intensity image of the sample. The labelled cells are visualized clearly by the microscope image while the unlabeled cells are invisible. Figure. 16b shows the dsRed exogenous fluorescence image acquired by our system. The labeled cell region (above) is successfully visualized while the un-labeled cells (below) cannot be resolved. However, from the lifetime image (Fig. 16c), both labeled and un-labeled cells seeded regions were found with lower lifetime compared to AR-BP tissue. This is a good proof to our system's performance that FLIm modality successfully captures the endogenous fluorescence from cells without the need of using any label.

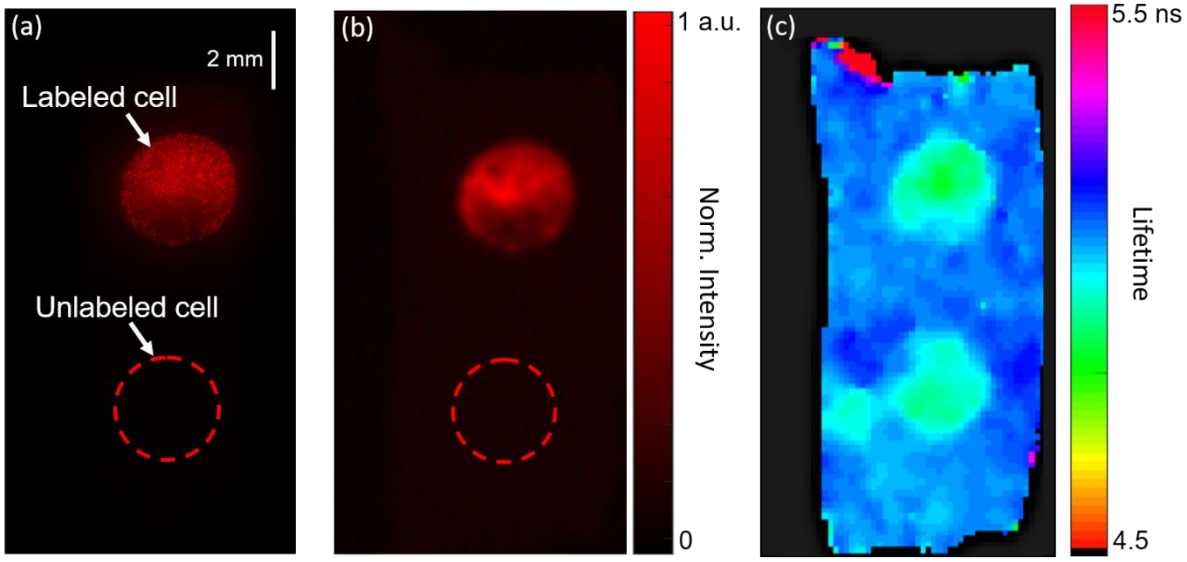

Figure 16. Images of dsRed-hMSC seeded antigen removed bovine pericardium representative sample. (a) Fluorescence microscopy image of the flat sample before suturing. (b) Normalized dsRed fluorescence intensity intraluminal image of the same sample inside the bioreactor. (c) Corresponding intensity weighted fluorescence lifetime intraluminal image at SB3 (532 - 553 nm).

3.2.6 Discussion

In this study, we present a fluorescence imaging system that seamlessly couples with a

bioreactor for intraluminal imaging of developing TEVG. We demonstrated the system's ability to simultaneously acquire fluorescence lifetime images with co-registered exogenous fluorescence intensity images of tubular phantoms with enough resolution to detect tissue level contrast (Fig. 14). The FLIm module has the sensitivity to resolve cellular fluorescence from natural matrix fluorescence background non-destructively (Fig. 15d and 15e). Our previous studies have shown the capabilities of this FLIm system to monitor tissue level property changes using all four spectral bandwidths (SB) [62], [82], [89]. After demonstrating the system capability for capturing weak cellular fluorescence, we anticipate that the integration with the bioreactor will enable monitoring properties of maturing TEVG inside the bioreactor non-destructively. Different from previously reported methods, which either modified graft fabrication procedures in favor of imaging or can only provide structural information [49], [78], [80], our system can provide biochemical information about the composition of tissue as well as cellular activity without compromising the TEVG fabrication processes inside a bioreactor. To validate endogenous FLIm results, the current exogenous fluorescence modality is configured to detect eGFP (Fig. 15c), further validated with conventional fluorescence microscopy of the flat sample prior to suturing (Fig. 15b). It is easy to adapt the exogenous fluorescence modality to any fluorescence label of interest (Fig. 16), making it a suitable tool for either validating findings from endogenous fluorescence images or providing extra information related to cell-tissue interactions.

3.2.6.1 Imaging speed

As opposed to conventional intravascular imaging that requires fast scanning speeds typically achieved by using a fiber optic rotary joint, imaging inside a bioreactor is more tolerant to slow scanning speed. Therefore, helical scanning was performed by reciprocally rotating the

optical fiber bypassing a fiber rotary joint that introduces extra transmission losses [90], compromising detection of cellular fluorescence. For this iteration of the instrument, we focused on increasing the sensitivity by capitalizing on high averaging, namely 64 waveforms for each pixel, which resulted in an increased signal to noise ratio (SNR) but also an increase of data acquisition (DAQ) time. The DAQ time includes data acquisition, pulling data from digitizer, PMT gain controlling, real time waveform display, and saving for a single pixel. The fastest performance of the current instrument is achieved by running the UV excitation laser at its maximum repetition rate, but this time is increased by synchronizing the reflective optical chopper wheel (ROCW) rotation to the UV excitation laser pulse. Using a 10 slot ROCW with the chopping frequency at 1 kHz, the present DAQ time was around 80 ms and the scanning speed was 4 rpm. A 20 mm vascular graft was fully covered in 20 min with an axial step size of 200 μm and a lateral step angle of 5°. In future work, the scanning speed can be improved by burst pulsing the UV excitation laser to asynchronously acquire endogenous FLIm and exogenous fluorescence intensity images or directly increasing the chopping frequency to match the laser maximum repetition rate using a ROCW with more slots. Another significant change may involve more sensitive detectors to reduce the number of waveforms averaging for each pixel. Nonetheless, the ultimate application for this instrument was using the endogenous fluorescence lifetime modality to monitor vascular graft maturation processes, so it is expected that the imaging speed will not be limited by the ROCW.

3.2.6.2 Side viewing imaging probe

Another critical aspect of the current instrument is the side viewing optical fiber probe. The current probe was a 400 μm core multimode optical fiber with its distal end polished to 41° without reflective coating. By inserting the optical probe to a transparent glass imaging tube

that provides an air interface, the light reflection is realized by total internal reflection on the angled polished surface. Using this probe, the output average laser power was 0.70 mW for the endogenous fluorescence modality (355 nm pulsed laser, 1 kHz repetition rate) and 0.70 mW for exogenous fluorescence modality (440 nm cw laser modulated by ROCW at 1 kHz with 50% duty circle). Comparing with an enface viewing optical fiber of the same characteristics, the angled surface introduced a loss of -0.81 dB, likely due to light leaking through the angled polished surface by refraction. In addition, although the probe resolution was adequately suitable for this tissue level study as demonstrated with the stent phantom (Fig. 14d-e), it was not comparable to those using distal optics like GRIN lens or free-form optics [91], [92] because of beam divergence. However, with no component added at the distal end, the current probe had the fluorescence background as clean as a bare fiber at UV light excitation and less throughput loss at the interfaces. This is important for high sensitivity applications such as the detection of weak cellular fluorescence in tissue. To improve the optical performance without reducing system sensitivity, future work will explore the possibility of fusion splicing a silica-based ball lens or free form optics to the distal end of this multimode fiber [93].

3.3 Conclusion

In this chapter, we reported the development of an endogenous FLIm and exogenous cw fluorescence imaging system for intraluminal imaging of the TEVG inside the bioreactor. This system permits the scanning of TEVG luminal surfaces in their maturing environment (inside a bioreactor), acquires time-resolved fluorescence images from tissue endogenous fluorophores for sensitive detection of biochemical features, and enables co-registration of each measurement with fluorescence derived from exogenous molecular probes (e.g., eGFP, dsRed). Benefiting from its non-destructive *in situ* nature, this dual-modality system provides

a valuable research tool for tissue engineering studies of cell-tissue interactions and ECM properties monitoring in three-dimensional culture conditions, such as exploring mechanisms of tissue remodeling and recellularization, as well as optimizing protocols for fabricating TEVGs.

Chapter 4: Optical imaging system for non-destructive monitoring of vascular graft after implantation

4.1 Introduction

Failures of implanted tissue engineered vascular graft may occur due to thrombosis, intimal hyperplasia, or formation of atherosclerosis plaque [6]. For successful clinical use of TEVG, it is important to study its post-implementation performance and establish any possible causes of vascular graft failure. Clinical imaging techniques like CT, MRI and PET have been used to monitor the patency rate of TEVGs after implantation [94]. However, the instrumentation required for these techniques is too expensive to be extensively applied for tissue engineering studies. In addition, some modalities like PET require additional contrast agents, increasing the complexity of vascular graft manufacturing and challenging clinical regulation [78]. Intravascular imaging, which directly scan the intraluminal surface of vessels with optics or ultrasound, is currently a popular method for diagnosing and studying cardiovascular diseases [95]. Many studies have utilized these techniques to investigate the progression of cardiovascular diseases like atherosclerosis, which features changes in structural properties (lumen diameter, tissue morphology) and biochemical compositions (lipid, calcium, collagen, elastin) [96]. Therefore, we propose to use intravascular imaging to study the causes of failure of TEVG after implantation. The following sections discussed different intravascular imaging techniques that have been developed for this purpose.

4.1.1 Intravascular ultrasound (IVUS)

Ultrasound imaging visualizes the tissue structure by sending an ultrasound pulse to the sample and measuring the reflected attenuated signal that is modulated by the scattering of tissue. For intravascular ultrasound (IVUS) imaging, the generation and receiving of the ultrasound wave are performed by a single component called transducer. It is made from

piezoelectric crystal material that can expand and contract based on the applied electric signal. Compared with optical imaging, ultrasound imaging can visualize structures deeper inside the tissue, because ultrasound waves penetrate tissue for longer distance. The penetration depth of IVUS is typically beyond 10 mm, enabling it to profile the whole vessel wall [97]. However, the spatial resolution of IVUS is not as good as optical imaging. For an IVUS system working at frequency of 20 to 40 MHz, the imaging resolution is around 80 μm in the axial direction and 250 μm in the lateral direction [98]. This poor resolution limits its use as a structural imaging modality since it cannot visualize smaller features like micro-cavities, collagen fibers, or accurately measure the lumen openings [99].

4.1.2 Intravascular optical coherence tomography (OCT)

Optical coherence tomography (OCT) is currently the most popular optical imaging technique used for intravascular imaging because of its excellent spatial resolution (10 μm both laterally and axially). In addition, since intravascular OCT uses near infrared (NIR) light, it has the best penetration depth among all the optical imaging techniques (1-2 mm) [44]. Therefore, OCT has been used for many studies to investigate cardiovascular diseases, providing plenty of evidence that intravascular OCT can visualize the intimal thickening, fibrous plaque, calcifications, macrophage accumulation, thrombosis, and many other vessel disorders [100]. However, like IVUS, intravascular OCT only monitors the structural properties and cannot detect changes of biochemical composition in vessels. To complement this, some special OCT modalities have been developed from intensity-based OCT such as polarization sensitive OCT (PS OCT) that can measure the collagen content, and optical coherence elastography (OCE) that can measure the mechanical strength of the vessel [53], [54].

4.1.3 Intravascular near infrared fluorescence (NIRF) and near infrared autofluorescence (NIRAF) imaging

Currently, researchers are looking for complementary optical imaging modalities that can measure tissue or cellular biochemical properties. As discussed in previous chapters, fluorescence imaging measures the fluorescent emission from certain biochemical components that are introduced externally or naturally exist in tissues. In terms of instrumentation, it is relatively simple to combine a fluorescence intensity detection modality to existing optical systems. By introducing a near infrared fluorescence (NIRF) agent, vessel disorders related to high-risk plaque, like protease, foamy macrophages, and intra-plaque hemorrhages, can be detected by NIR fluorescence imaging [101], [102]. A near infrared autofluorescence (NIRAF) imaging was also developed to facilitate structural imaging and one study showed that the measured NIR signal was associated with high-risk plaque sites [103]. But like PET, this addition of NIR fluorescence agents increases the complexity of TEVG studies.

4.1.4 Intravascular FLIm

The previous chapters introduced that autofluorescence can be excited by ultraviolet (UV) light from various biochemical components such as collagen, elastin, and free or bound NADH [58]. Multiple studies have demonstrated that the multi-spectral fluorescence lifetime imaging (FLIm) system can be applied for non-destructive monitoring of tissue and cellular properties [62], [82]. In addition, an intravascular FLIm system was combined with IVUS [104] and it was used to show that FLIm can visualize the atherosclerotic lesions in human coronary arteries by detecting biochemical components including accumulation of foamy macrophages, extracellular lipids, and superficial calcium [105].

4.1.5 Multimodal imaging

Table. 2 summarizes and compares the characteristics of the intravascular imaging modalities as described above. Nowadays, IVUS and intravascular OCT are the most popular techniques for intravascular imaging and consensus for guiding the use of both modalities were made according to the results from a large number of studies [98], [100]. Along with the wider use of IVUS and intravascular OCT, molecular imaging techniques like NIRS and FLIm are being investigated to uncover their diagnostic potential and their ability to study the progression of cardiovascular diseases [102]. Currently, there is a trend of developing multi-modal systems combining different imaging techniques. For example, IVUS and NIR spectroscopy (IVUS and NIRS) was developed to examine plaque anatomy and lipid components [106]. NIRAF was added to OCT to better detect the high-risk plaque [103]. Both IVUS and OCT were combined with FLIm to measure biochemical and structural properties of vessels [104], [107]. IVUS and OCT were also combined to benefit from their complementary penetration depth and spatial resolution [108]. In this chapter, an intravascular FLIm and OCT system was designed and built based on the system described in previous chapters, with a custom fiber optic rotary joint (FORJ) and a catheter using micro-optic (U optic). The performance of each modality will be described and discussed in the following sections. To validate the system performance, a tubular fluorescent phantom and a decellularized venous conduit were imaged with this multi-modal system.

Table 2: Comparison of characteristics of different intravascular imaging techniques. * indicates better performance and more evidence. - indicates not suitable or no evidence has been observed [102]–[104], [107], [109]–[111].

Measure	IVUS	OCT	NIRF&NIRAF	FLIm
Spatial resolution	100 μm	10 μm	100 μm	100 μm
Tissue penetration	>5 mm	1-2 mm	-	-
B-Scan speed	20-30 Hz	100 Hz	100 Hz	30-100 Hz
Visualize	Anatomy	Anatomy	Biochemistry	Biochemistry
Need flushing blood	no	yes	yes	yes
Cap thickness	*	**	-	-
Plaque burden	**	*	-	-
Calcification	***	**	-	**
Lipids	*	**	*	**
Macrophages	-	*	*	***
Necrotic core	**	**	*	*
Cholesterol crystals	-	-	**	-

4.2 Intravascular FLIm and OCT system

4.2.1 System design

Figure. 17 shows the schematic of the intravascular FLIm and OCT system that was designed. It is mainly composed of four parts: 1) FLIm modality, 2) OCT modality, 3) Motor Drive Unit (MDU) and 4) Catheter made from a double clad fiber (DCF). Based on this, a prototype system was built in the laboratory for proof of concept. The following sections will describe each modality of the prototype system in detail.

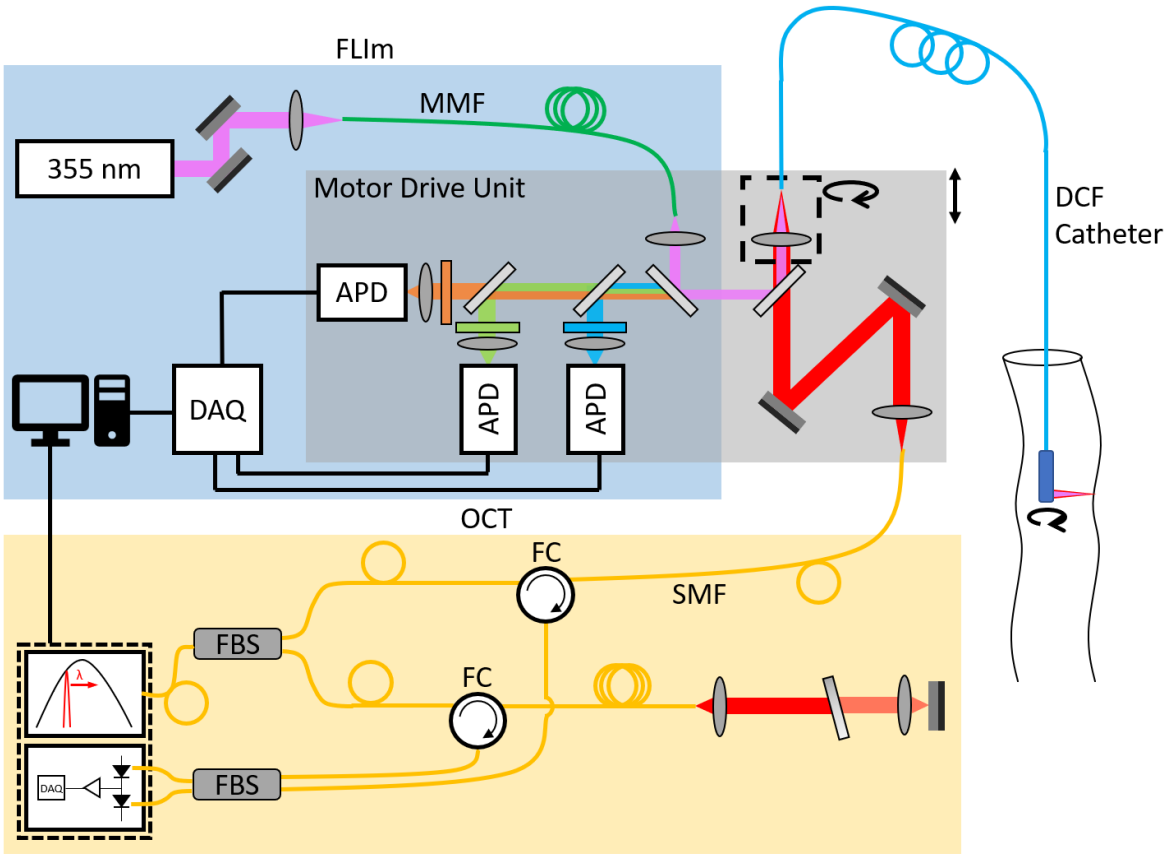

Figure 17. The schematic of the Intravascular FLIm and OCT. It is mainly composed of four parts: FLIm modality, OCT modality, motor drive unit (MDU) and a double clad fiber (DCF) based catheter. MMF: Multimode fiber, APD: Avalanche photodiode, DAQ: Data acquisition module, FC: Fiber circulator, FBS: Fiber beam splitter, SMF: Single mode fiber.

4.2.1.1 FLIm modality

As shown in Fig. 17, FLIm excitation is performed by a 355 nm UV pulsed laser (STV-02E, TEEM photonics, France). The excitation light is coupled to a 50 µm core, multimode optical fiber (MMF) and guided to the MDU. The light is then coupled to the catheter through the MDU and finally guided to the tissue sample. The excited fluorescent light is collected by the catheter and coupled back to the MDU. The MDU includes a wavelength selection module (WSM) composed of three dichroic beam splitters and bandpass filters. The fluorescent light is divided into three spectral channels (Channel 1: 390/40 nm, Channel 2: 435/40 nm, Channel 3: 510/84 nm) and focused to three avalanche photodiode (APD) detectors. Compared with

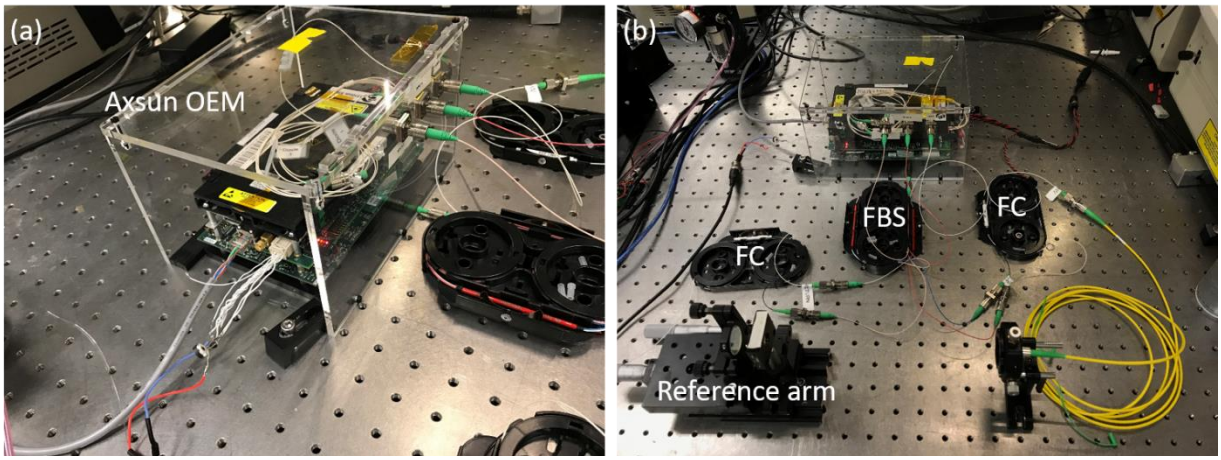

Figure 18. Photos of OCT modality. (a) close look of the Axsun OEM module including the swept-wavelength light source, balanced detector, A/D converter and firmware programmable gate array (FPGA). (b) The image showing OCT modality including the OEM, fiber optics and free space optics for reference arm. FC: fiber circulator, FBS: fiber beam splitter

the previous FLIm system using a photomultiplier tube (PMT) detector, the use of APD improves the signal-to-noise ratio (SNR) and further increases the acquisition speed for FLIm. Since APDs are very compact, we designed the FLIm modality to directly couple fluorescent light to the APDs placed inside the WSM. This avoids the use of relay fibers like the previous FLIm system (Fig. 2) that cause additional loss of optical signal. The fluorescence dynamics are then recorded using high speed digitizers operating at the sampling rate of 6.25 GS/s (PXIe-5185, National Instruments, Austin, TX). The fluorescence intensity and lifetime can be derived from the recorded fluorescence decay using the algorithm described in previous chapters [63].

4.2.1.2 OCT modality

The OCT modality is built based on an integrated Opto-electro-mechanic (OEM) module from Axsun Tech Inc. (Billerica, MA, USA) that includes the swept-wavelength light source, balanced detector, A/D converter and a firmware programmable gate array (FPGA) (Fig. 18a). The light source is centered at 1310 nm and has 100 nm of the spectral bandwidth. The IR light from the OEM light source is coupled to a 90/10 fiber beam splitter (FBS) as shown in

Fig. 17 and 18b and divided in power so that 90% of light enters the sample arm and 10% enters the reference arm. In the reference arm, the light is coupled to the fiber circulator (FC) and guided to a collimator. The collimated light is then reflected in free space by a mirror mounted on a linear stage and coupled back to the FC. The FC has three ports and couples the reflected reference light to a 50/50 FBS. In the sample arm, the IR light is coupled to another FC and guided to the MDU with a single mode fiber (SMF). It is then coupled to the catheter through the MDU and guided to the tissue sample. The IR light penetrates through the tissue and is backscattered from the different layers in tissues. These backscattered photons are collected by the catheter and coupled back to the OCT modality through the MDU. Like the reference arm, the sample light is guided back to the FC and finally enters the 50/50 FBS. The lights from both arms interfere inside the FBS and the interference signal is sent to the balanced detector in the OEM [112]. The signal is sampled by an A/D converter triggered by a built-in k-clock so the spectrum of interference can be recorded. The spectrum is then processed by the on-board FPGA, and the processed results are transferred to the computer for analysis. For each spectrum, the profile of backscattered intensity over different depths in the tissue is generated. This shows the tissue structure along the axial direction and is referred to as A-scan. By rotating the catheter to scan the IR light along the transverse direction, the cross-section image of the tissue can be acquired and is referred to as B-scan. In the end, a 3D volumetric image can be generated by pulling back the catheter to acquire B-scans at different axial locations.

4.2.1.3 Motor drive unit

The motor drive unit (MDU) is the component that rotates and pull back the catheter to mechanically scan the light across the vessel's intraluminal surface. In this system, the MDU includes two parts. One is the wavelength selection module (WSM) as described in the FLIm modality. The other is the fiber optic rotary collimator (FORC) that couples the light from both FLIm and OCT modalities into the catheter, as shown in Fig. 19a. The FORC is composed of a custom designed hollow shaft (Fig. 19b) that is constrained by an air bearing (OAV0500IB, OAV air bearing, Princeton, NJ). The head of the hollow shaft holds an un-coated aspheric lens (A397-UC, Thorlabs, Newton, NJ) to focus the collimated beam from OCT or FLIm modalities to the double clad fiber (DCF) in the catheter. The lens to fiber distance is optimized by shimming washers between the two components and the lateral position of the lens is adjusted by the four set screws surround it (Fig. 19b). A FC/PC receptacle is mounted on the hollow shaft so the catheter can be connected to the FORC by a FC/PC connector. The rotation of FORC is performed by attaching a pulley belt on the shaft that is driven by a motor on the side. As shown in Fig. 19a, the FORC with other components

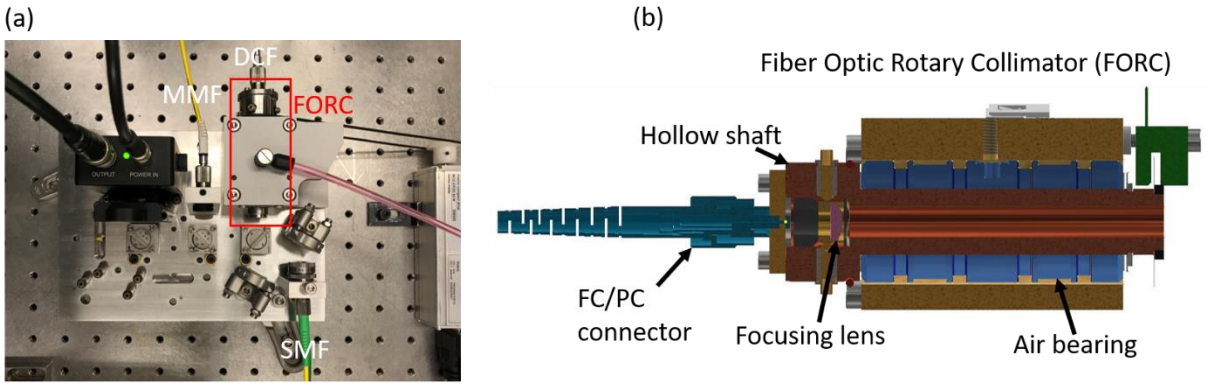

Figure 19. Motor drive unit. (a) The prototype of motor drive unit for testing. The red rectangle includes the fiber optic rotary collimator (FORC). (b) The cross-section schematic of the FORC. It includes a custom hollow shaft that is mounted on an air bearing. The distal end of the shaft holds an aspheric lens inside. A FC/PC receptacle is mounted to the shaft so the catheter can be connected by a FC/PC connector

together is mounted on a stainless-steel subplate that can be pulled back using a linear axis stage. In this way, the catheter can be rotated and pulled back by the MDU to realize the helical scanning.

4.2.1.4 Catheter design

As shown in Fig. 17, the catheter, interfacing between the system and the samples, is a flexible probe that can be inserted into the vessel for intraluminal imaging. The core of the catheter is

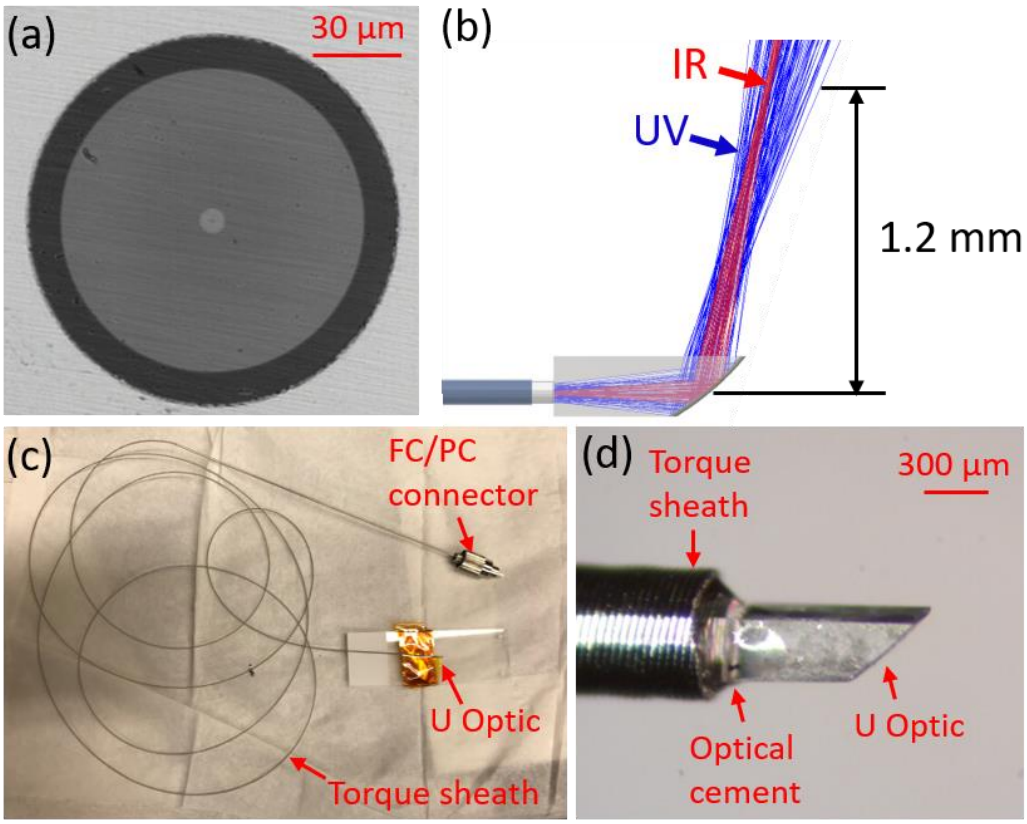

Figure 20. Catheter design. (a) bright field image showing the end face of a double clad fiber (DCF) inside a FC/PC connector. The small circle in the center is the core (bright). Towards the outside, there are inner cladding (intermediate) and outer cladding (dark). (b) The schematic showing the ray tracing simulation of the micro-optic (U Optic) probe in Zemax. The IR light from the core of DCF is focused at 1.2 mm away from the probe axis. (c) The white light image showing the fabricated catheter. The distal end of the catheter is U Optic. The DCF is inserted through a 1.6 m torque sheath that can transfer the torque from proximal end to the distal end. The proximal end of the catheter is a FC/PC connector that will be connected to the fiber optic rotary collimator (FORC); (d) The microscope image showing the distal end of the catheter. The U Optic is attached to the DCF with UV curing optical cement.

a double clad fiber (DCF, Nufern 9/105/125, East Granby, CT). Figure. 20a shows the end face of a DCF inside a FC/PC connector. Different from a normal SMF or MMF, the DCF has three layers: core (small circle in the center), inner cladding (intermediate ring) and outer cladding (the dark ring outside). In this DCF, the core is designed to be single mode for IR with a 9 μm diameter while the inner cladding is multi-mode with a diameter of 105 μm. The existence of an additional outer cladding (125 μm diameter) enables the inner cladding to guide the light. To maintain the coherence of light for OCT imaging, the IR light is guided through the single mode core. For FLIm, both excitation and emission light are guided through the inner cladding because of its larger numerical aperture (NA).

In addition to the fiber, another key component of the catheter is the distal optic that reflects and focuses the light from the DCF to the vessel wall. As shown in Fig. 20b, a monolithic micro-optic (U optic) is attached to the optical fiber with a reflective surface on the distal end. This reflective surface is coated with aluminum and has an ellipsoid profile so it can reflect and focus the light at the same time [113]. By simulating in Zemax, we optimized the design of the U optic so that the IR light can be focused 1.2 mm away from the probe axis (Fig. 20b). This working distance is determined based on the diameter of a typical coronary artery (2.5 – 3 mm). As shown by the simulation result (Fig. 20b), a waist difference of around 0.5 mm is found between UV and IR light. This difference is likely caused by the NA difference between the core (0.14) and the inner cladding (0.22). Figure. 20c and d show a catheter fabricated in the laboratory. The U optic is attached to the DCF with UV curing optical cement (OG603, Epoxy Technology, Billerica, MA). A custom CMOS based beam profiler was used to check the IR beam profile before the cement was cured by a UV lamp. After curing, the DCF was inserted through a 1.6 meter torque sheath (Asahi Intecc Co., LTD., Japan) and a 15 mm

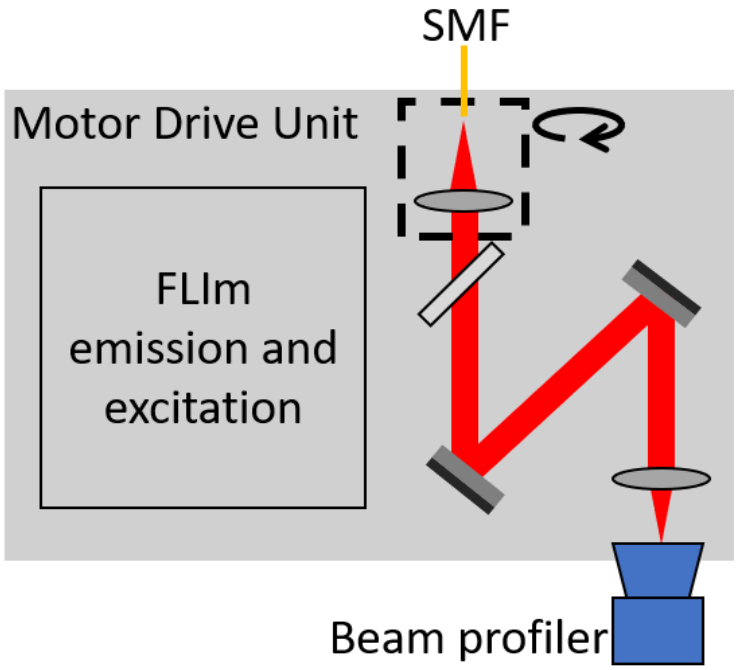

Figure 21. Schematic of the setup for examining the eccentricity of the FORC

stainless-steel hypodermic tube (Fig. 20c). The distal end of the DCF is also fixed to the torque sheath with the UV curing optical cement (Fig. 20d). Finally, the proximal end of the catheter is connectorized with a FC/PC connector (Fig. 20c).

4.2.2 Materials and methods

4.2.2.1 FORC throughput stability

The throughput stability of the FORC when it is rotating at high speed is important for the quality of the FLIm and OCT image. A severe decrease in throughput will lead to low signal to noise ratio (SNR) for both modalities, which will cause further problems like inaccurate lifetime calculation and ghost artefacts in the OCT images. To maintain a high and stable throughput during rotation, we need to minimize the eccentricity in FORC between the optical axis of the lens and the fiber, and the rotating axis of the shaft. The eccentricity between these two axes will make the beam move laterally and this lateral shift will cause the throughput of UV and IR light to oscillate during the rotation of the FORC. To examine the eccentricity, we

connected a single mode fiber (SMF) to the FORC that coupled the IR light from the OCT modality. A CMOS based beam profiler was placed on the receiving end to monitor the focused IR beam movement (Fig. 21). The beam centroid coordinates were calculated for each frame taken by this beam profiler and recorded when the FORC was rotating. The eccentricity was then quantified by calculating the standard deviation of these beam centroid coordinates. Based on this, we aligned the lens and fiber inside the FORC to minimize the eccentricity. To estimate the influence on throughput from the lateral shift of beam centroid, we performed a tolerance analysis using Zemax. The throughput versus the distance between the beam centroid and the fiber core was calculated. Finally, the IR throughput was measured by connecting a short piece of SMF to the FORC and placing a power meter on the distal end of this short SMF. The power meter has an analog output corresponding to the measured power that is connected to an oscilloscope (PXI 5114, NI, Austin, TX). The throughput of IR was calculated by dividing the output after the short SMF by the power before the FORC. A waveform of IR throughput was recorded when rotating the FORC at 10 rounds per second (rps). Similarly, the UV throughput was measured by using a short MMF (105 μm core diameter).

4.2.2.2 Catheter beam profile

The beam profile of the UV and IR beam from the catheter will determine the properties of our imaging system including the working distance, spatial resolution, and field of view. The aberrations from the distal optics can also be visualized by measuring the beam profiles. To do this, we mounted the CMOS based beam profiler on a linear axis stage and recorded the beam profiles of the UV and IR light from the catheter at different distances away from the probe axis. The full width at half maximum (FWHM) was calculated from the beam profiles

along both axial and tangential directions.

4.2.2.3 Phantom

A tubular fluorescent phantom was made by inserting a drug eluting stent into a 3 mm I.D. fluorescent PMMA tube as shown in Fig. 24a. The imaging was performed by inserting the catheter into the stent and filled the phantom tube with phosphate buffer saline (PBS). A 5 mm section of this phantom was scanned by the system with an axial step size of 50 µm. To demonstrate the co-registration of FLIm and OCT images, the normalized fluorescence intensity image was compared with the intraluminal 2D OCT map that was obtained from the OCT 3D image averaged along the axial direction with each pixel value representing the averaged intensity of the corresponding A-scan.

4.2.2.4 Biological sample

A 5 cm long fresh bovine saphenous vein (SV) was harvested from young adult cattle (Fig. 25a). It was dissected to remove perivascular connective tissue and adventitia. The SV was then decellularized by the process called antigen removal that was described in previous work from H. Lopera et al. [114]. Compared with the conventional sodium dodecyl sulfate (SDS) decellularization, this method better maintains the collagen and elastin macromolecular structure and showed much less cellular toxicity [114]. Like imaging the phantom, the SV was scanned by the catheter at an axial step size of 50 µm. The rotation of the catheter was set at 5 rps, limited by the FLIm laser repetition rate.

4.2.3 Results

4.2.3.1 FORC eccentricity and throughput

Figure. 22a shows the IR focused beam on the receiving end taken by the beam profiler. The beam centroid was marked by a small red circle in the center. A gaussian profile was observed

for the beam with most energy confined within the 9 μm diameter red circle corresponding the size of a single mode fiber (SMF) core (Fig. 22a). If the SMF core aligns with the centroid of the beam, the throughput will be maximized. However, during the rotation, the beam centroid moved laterally due to the eccentricity of the FORC, and this lateral shift will decrease the throughput. The calculated IR throughput versus the distance between the beam

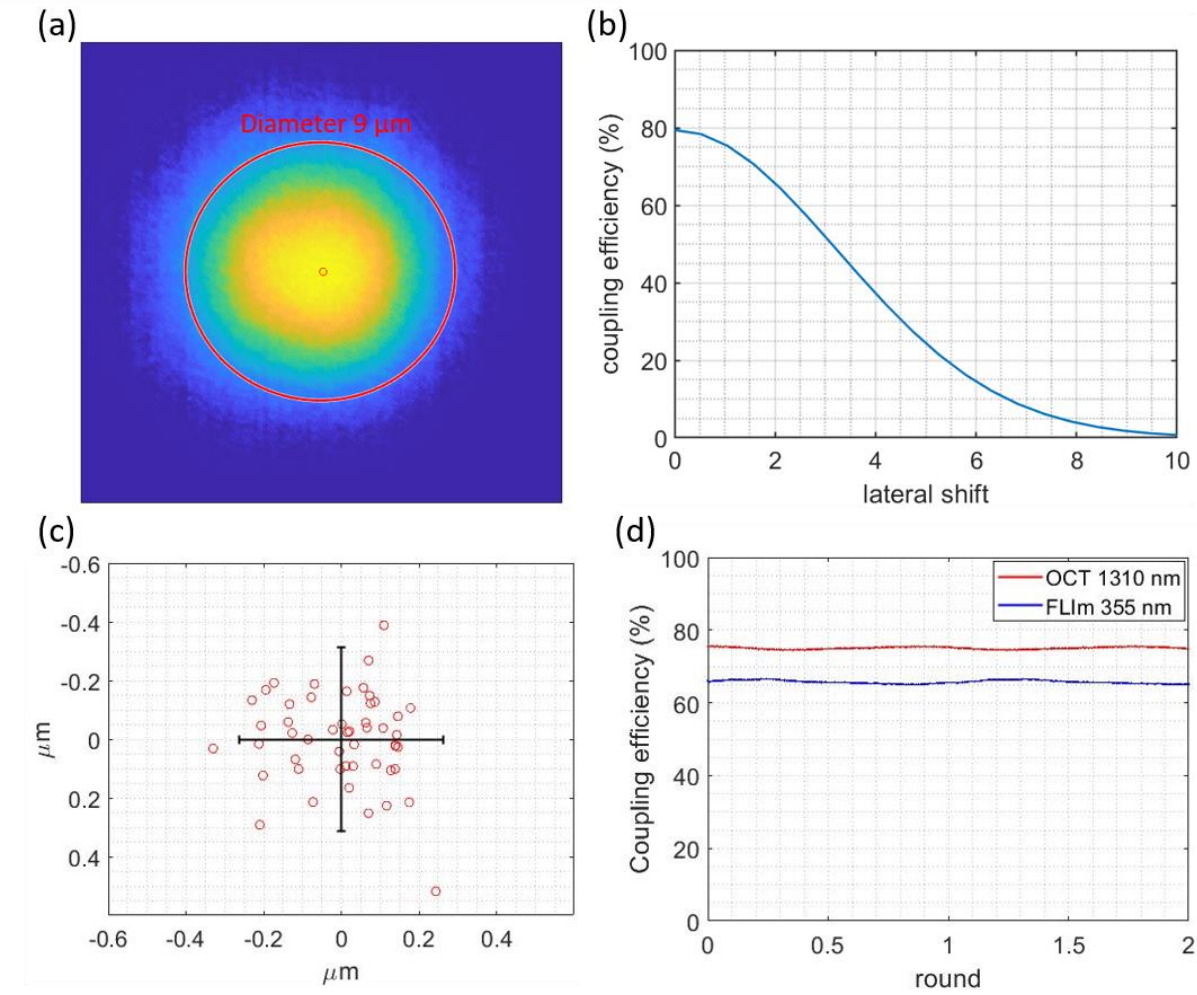

Figure 22. Results of the eccentricity and throughput measurements. (a) the beam profile recorded by the beam profiler. The large red circle corresponds to the size of a single mode fiber (SMF) core. The small circle in the center represents the calculated beam centroid. (b) The calculated IR throughput versus the distance between the beam centroid and SMF core from 0 to 10 μm. (c) The record of beam centroid locations during the rotation of FORC. The half width of the error bars is 0.3 μm for horizontal direction and 0.4 μm for vertical direction. This was recorded after optimizing the alignment of FORC. (d) The throughputs for UV and IR beam during the rotation.

centroid and SMF core is shown in Fig. 22b. Figure. 22c shows the recorded beam centroid locations over a few rotations after the eccentricity was minimized by aligning the lens and fiber inside the FORC. From this, we can calculate the standard deviations of the beam centroid coordinates, which are 0.15 μm for the horizontal direction and 0.2 μm for the vertical direction. The error bar on Fig. 22c with the length of 0.3 μm horizontally and 0.4 μm vertically includes over 95% of the recorded beam centroids. Therefore, for this system, the maximum lateral shift during rotation is around 0.4 μm, if the SMF core is located at the center of the beam centroid trajectory. By finding the throughput when the lateral shift is 0.4 μm from the tolerance analysis (Fig. 22b), we expect the IR throughput to be around 76-77% during the rotation of the FORC. Figure. 22d shows the measured throughput for both IR and UV during the rotation. The IR throughput is centered at 75% with a variance less than 1% which is very close to our expectation and the theoretical maximum throughput of 79%. In addition, the UV throughput is centered around 65% with a variance of less than 2%.

4.2.3.2 Beam profile

Figure. 23a shows the beam profiles of UV and IR light at different distances away from the probe axis. Both the UV and IR beam look clean and symmetric, indicating only small aberrations from the U optic. Fig. 23b shows the full width at half maximum (FWHM) of UV and IR light at the distance recorded from 0.2 to 3.2 mm. It shows that the waist of the IR beam is located at around 1.2 mm away from the probe axis, which is consistent with the simulation result (Fig. 20b). The axial field of view (FOV) for OCT can be determined by finding the depth of field (DOF), defined as the distance from the waist where the beam cross section area doubles. From the FWHM plots, the FOV is around 0.8 mm for our system. Some astigmatism is observed for the IR light corresponding to the waist difference (around 0.2

mm) between the axial and tangential direction. There is almost zero astigmatism for UV light, but the waist is located around 0.6 mm closer to the probe axis compared with the IR waist. This waist difference between the UV and IR light is also consistent with the simulation result as shown in Fig. 20b.

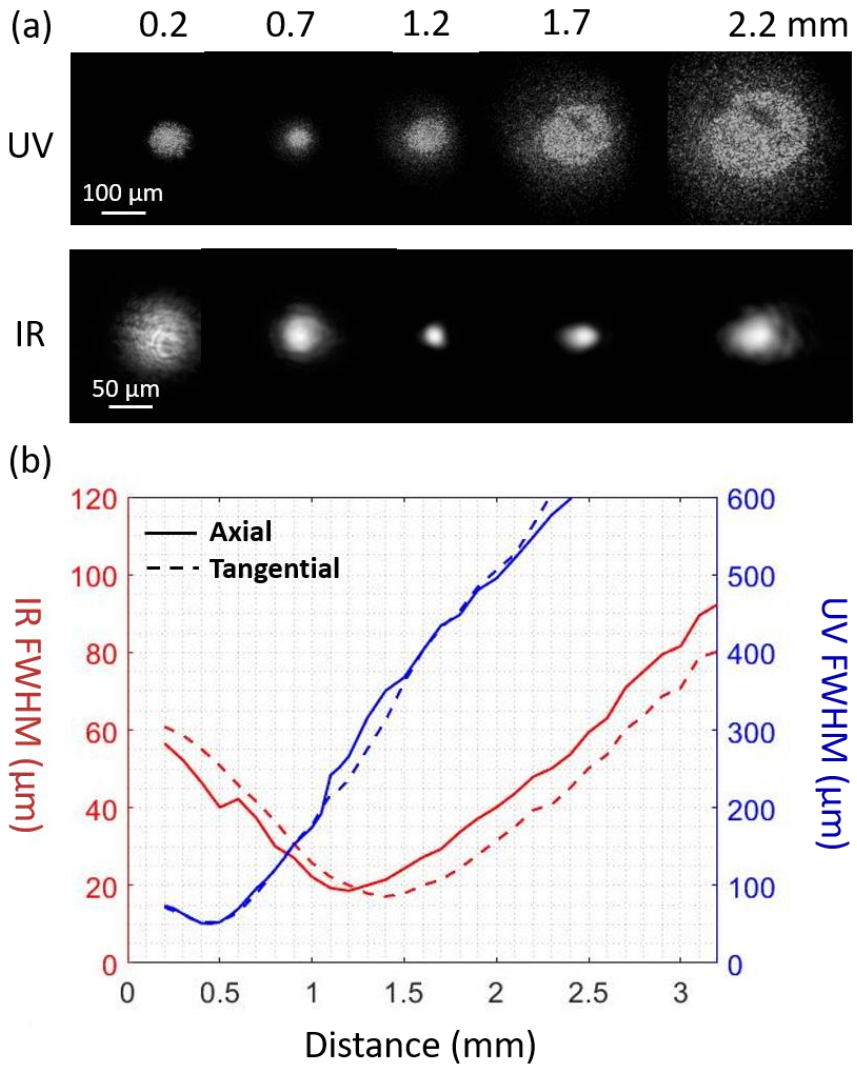

Figure 23. Results of catheter beam profiling. (a) The UV and IR beam profiles at the distance of 0.2, 0.5, 1.2, 1.7 and 2.2 mm away from the probe axis. (b) The full width at half maximum (FWHM) for both axial and tangential directions at distance of 0.2 – 3.5 mm away from the probe axis. The red color represents the results for IR and the blue color represents the results for UV

4.2.3.3 Phantom Image

Figure. 24b-d show the FLIm and OCT images of the tubular phantom. The fluorescence

lifetime image is shown in Fig. 24b and the stent can be clearly visualized by the low lifetime regions. The fluorescence lifetime for the PMMA (the background) is around 3 ns, consistent with previous work [90]. Figure. 24c and d show the OCT projected intraluminal image and the FLIm normalized fluorescence intensity image. Both captured a sharp image of the embedded stent (~40 μm), indicating the good spatial resolutions for both modalities.

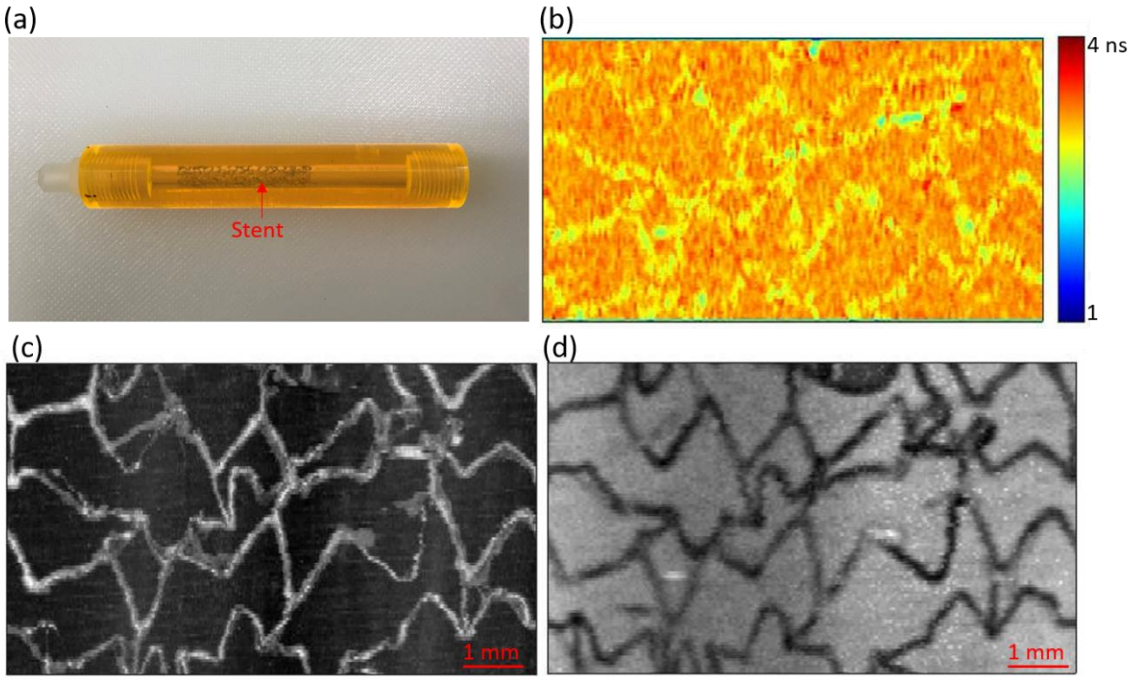

Figure 24. Results of phantom measurement. (a) Photo of the tubular fluorescent phantom. A drug eluting stent was inserted into a 3 mm I.D. fluorescent PMMA tube. (b) The intraluminal fluorescence lifetime image covering a section of 5 mm. (c) The OCT intraluminal image acquired by averaging the A-scans. (d) The intraluminal normalized fluorescence intensity image.

4.2.3.4 Biological sample

The images from the SV are shown in Fig. 25 and 26. Using the OCT modality, the 3D structure of SV can be visualized to show the shape and dimensions of this vascular graft (Fig. 25b). Since the FLIm and OCT images are co-registered, FLIm lifetime and intensity values can be mapped onto the OCT 3D structural image (Fig. 25c and d) to assess the biochemical properties along the vessel. Figure. 26 shows some representative OCT B-scan images. The

lumen diameter and tissue morphology were clearly visualized (Fig. 26a). In addition, the features like cavities and dwelling fibers inside the lumen can be easily found from OCT images (Fig. 26b and c).

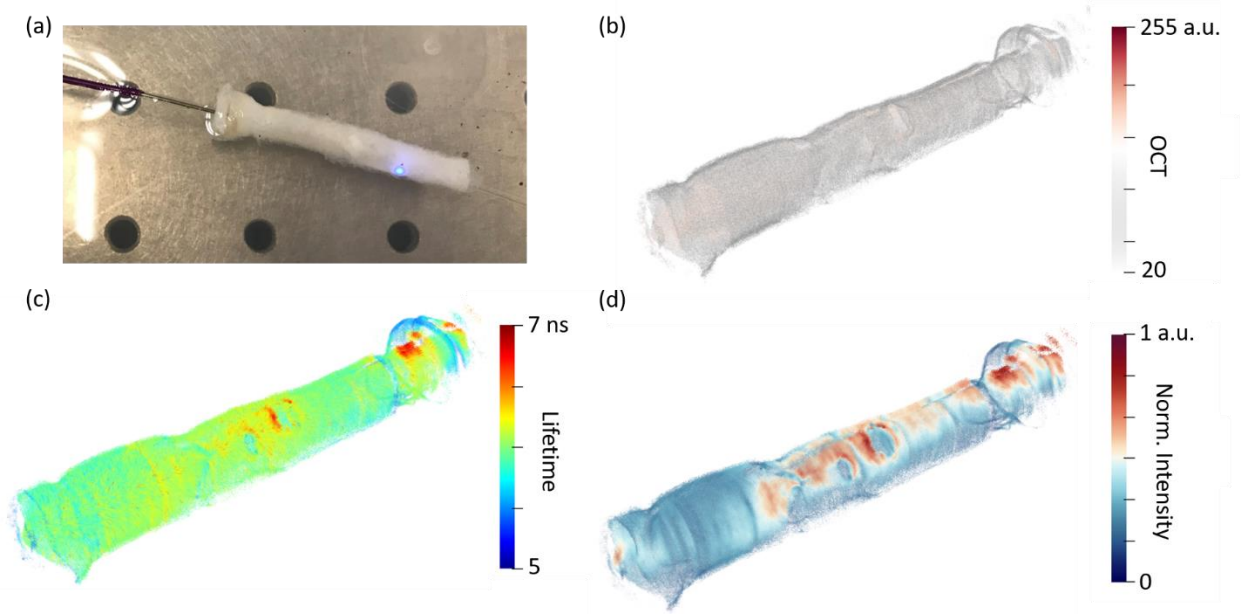

Figure 25. Results of antigen removed saphenous vein (SV). (a) photo showing that the SV was imaged by the intravascular FLIm and OCT system. (b) The 3D OCT image of the SV. (c) The 3D image of SV with the color coded by FLIm lifetime values. (d) The 3D image of SV with the color coded by FLIm normalized intensity values.

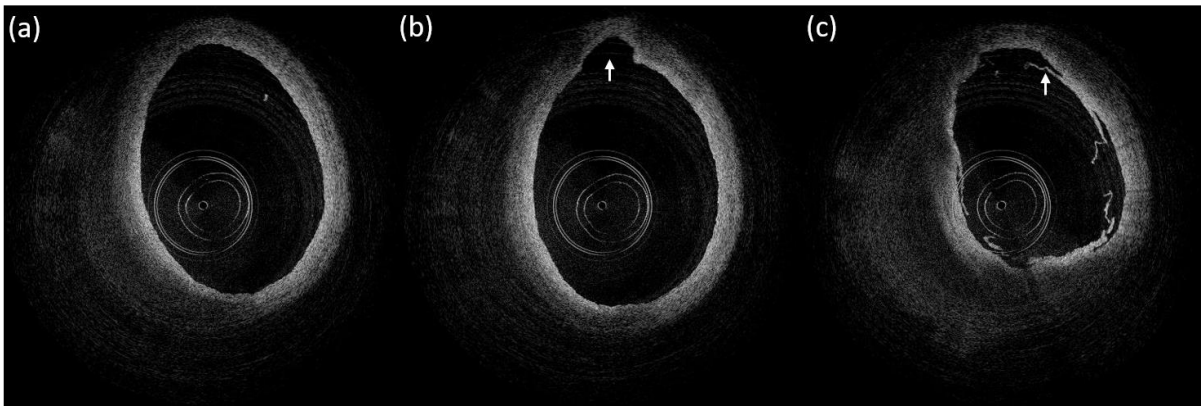

Figure 26. Representative OCT B-scan images showing the cross section of the saphenous vein (SV) at different locations. (a) The B-scan showing the tissue morphology of SV. (b) The B-scan showing a small cavity (white arrow) in the SV. (c) The B-scan showing the collagen fibers (white arrow) dwelling on the intraluminal surface

4.2.4 Discussion

In this chapter, an intravascular multi-modal imaging system was designed by combining

fluorescence lifetime imaging (FLIm) and optical coherence tomography (OCT). Demonstrated by the imaging results of tubular fluorescent phantom and antigen removed saphenous vein, this system is capable of monitoring the structural properties like lumen diameter and tissue morphology using OCT modality, and acquiring FLIm images that are known to relate the tissue biochemical and biomechanical properties [62]. Compared with other intravascular FLIm and OCT systems [107], [109], our design improves the system performances by achieving: 1) high and stable throughput during rotation for both IR and UV light (Fig. 22d); 2) outstanding beam performance by using the micro-optic (U optic).

4.2.4.1 MDU

The motor drive unit (MDU) is the component that realizes the intraluminal scanning by rotating and pulling the catheter. The challenge of building this MDU is enabling the light to be coupled between the catheter and the static optics when the catheter is rotating at high speed (100 rps). As mentioned in the system design section, it is important to maintain a high and stable throughput during the rotation to maximize the SNR and reduce the image artefacts. Previous works about the development of fiber optic rotary joint (FORJ) showed two potential designs. One is called the lens-less FORJ by connecting the proximal end of the catheter (DCF) to a static fiber, as described in Wihan Kim's work [115]. The connection was realized by inserting the catheter and the static fiber to a glass capillary from both ends. During the rotation, the lateral movement of the catheter is confined by the glass capillary and since the two fibers are placed close to each other, the loss is small when the light transmits from the catheter to the static fiber. The throughput of this design was measured to be over 90%. However, some lubricating media is needed between the two fibers to facilitate the rotation and its refractive index needs to match the optical fiber to avoid the loss of light due to specular

reflection. Wihan Kim et al. investigated different lubricating media and found that the media will cause fiber damages under UV excitation. In the end, Wihan Kim et al. proposed to use the water as the alternative to lubricating media, which may have stability issues since water evaporates easily, and refilling is needed. In another work by Min Woo Lee et al. [109], a different design of FORJ was proposed by collimating the beam with lenses between the catheter and the static fiber. This design complicates the device and increases the challenges in alignment, but it avoids the use of any lubricating media and allows the light to propagate for a long distance between the catheter and the static fiber. Our design of MDU is based on this second option by collimating the light from the catheter using the fiber optic rotary collimator (FORC, Fig. 19b). The long propagation distance allows us to use the dichroic mirror to combine the light from FLIm and OCT modalities in free space. Different from Min Woo Lee's work that guides the fluorescent light from the catheter to the photodetector using relay fibers, we directly coupled the fluorescent light to the APD detectors to improve the collection efficiency for FLIm emission detection.

4.2.4.2 Catheter

The catheter is an imaging probe that can be inserted to the tubular construct and guides the light from the system to the tissue samples and back. As described in the system design section, the catheter is made from a double clad fiber with the distal end attached by a small optics to reflect and focus the light to the vessel wall. Different designs of the distal optics have been studied for the development of intravascular OCT systems, for example, gradient index lens (GRIN) and ball lens [116]. A GRIN lens is a cylindrical glass rod with the refractive index continuously decreasing from the optical axis to the periphery. By carefully choosing the material and dimensions of the GRIN lens, it can focus the beam at different

distances. A micro prism can be glued to the distal end of the GRIN lens to realize the reflection of light. However, it is challenging to use the GRIN for this FLIm and OCT system because most glass materials used to make GRINs are fluorescent under UV excitation. Although the GRIN made from lithium doped silica has relatively small absorption in UV, the probe using this GRIN will have a long rigid body (>10 mm) to achieve the working distance of 1.2 mm, which is not applicable for *in vivo* measurement. The ball lens is another popular distal optics used for intravascular OCT. It is fabricated by splicing a no core fiber (NCF) to the DCF and then fusing the distal end of the NCF to form a spherical shape. It is then angle polished to reflect the light by total internal reflection [107], [109]. The working distance of this probe can be controlled by changing the curvature of the spherical surface. The drawback of using a ball lens is that a cap covering the distal ball lens is needed to protect the spherical surface during the rotation, and to provide the glass-air interface to realize the reflection and for focusing [107]. This cap will distort the beam spot by introducing aberrations like astigmatism. In this work, the distal optics is a reflective micro-optic (U optic) that has an ellipsoid surface on the distal end that is coated with aluminum. The working distance can be controlled by changing the curvature of the reflective surface. As shown in Fig. 23, the designed probe successfully achieves a working distance of 1.2 mm and the depth of field of 0.8 mm for IR light. A small astigmatism was observed for IR light but since no cap is needed, it still outperforms the ball lens, and it generates these symmetric beam profiles. The beam profiling results also showed that UV waist was located 0.6 mm closer to the probe axis than the IR waist. This waist difference was in fact helpful to achieve the best optical performance for this multi-modal system, because FLIm images the superficial tissues (<200 μm) while OCT visualizes the structure around 1 mm deep inside the tissue.

4.3 Conclusion

In this chapter, we reported the development of an intravascular FLIm and OCT imaging system that can be applied for *in vivo* measurements of vascular graft post implantation. The system scans the intraluminal surface of vessels to generate OCT 3D structural images and FLIm images that reflect both biochemical and structural properties of vascular graft. We expect this system to be a valuable tool for monitoring the properties of vascular grafts inside of patients, to eventually study failure mechanisms after implantation.

Chapter 5: Conclusion

Tissue engineered vascular graft (TEVG) of small diameter is still under investigation in terms of material selection and processing, maturation strategies, validation of its clinical functionality. [117]. In this dissertation, we described a set of optical imaging tools for non-destructive monitoring of the TEVG properties at all three stages of manufacturing.

In chapter two, a pairwise comparison study was performed to investigate the potential of using multi-spectral fluorescence lifetime imaging system (FLIm) to replace conventional destructive measuring techniques used for TEVG development. The antigen removed bovine pericardium (AR-BP) whose properties were altered by the process called collagenase degradation, were measured with both FLIm and conventional measurements (i.e., collagen assay, tensile test, histology). A strong correlation was found between the fluorescence parameters (lifetime, spectral ratio) and the conventional measurement results (collagen content, Young's Modulus, UTS). This indicates that FLIm is capable of non-destructively monitoring biochemical and biomechanical properties of the biomaterials used to make TEVGs.

In chapter three, a bioreactor was built where the TEVG can be cultured with controlled environment (e.g., temperature, humidity, CO_2) and with pulsatile flow condition. we adapted our FLIm system for *in situ* imaging the intraluminal surface of the TEVG when it is cultured inside the bioreactor. An exogenous continuous wave (cw) fluorescence imaging modality was also incorporated to the imaging system. To demonstrate the system performance, an eGFP-hMSC seeded TEVG was imaged inside the bioreactor with our system. The cellular presence can be clearly captured by the FLIm image, validated by the co-registered exogenous fluorescence image. Therefore, an endogenous and exogenous fluorescence imaging system has been successfully developed for monitoring TEVG inside the bioreactor and it is capable

of assessing the recellularization process for TEVG development.

In chapter four, an intravascular fluorescence lifetime imaging and optical coherence tomography (FLIm and OCT) system was designed for *in vivo* imaging of vascular graft. The system performance was evaluated with the prototype built in lab and by imaging an antigen removed saphenous vein. The addition of OCT modality can provide a high-resolution 3D image showing the structure of TEVG. With the FLIm image mapped to the OCT structural image, this multi-modal system is capable of providing a comprehensive image dataset to reflect the biochemical and structural properties of TEVG. Although clinical studies need to be performed to evaluate the system performance for *in vivo* imaging, we expect it to be a tool to understand the failure causes of vascular graft after implantation, which is valuable for optimizing the manufacturing of TEVGs.

Reference

[1] C. D. Mathers and D. Loncar, “Projections of Global Mortality and Burden of Disease from 2002 to 2030,” 2006. Accessed: Dec. 28, 2020. [Online]. Available: www.plosmedicine.org.

[2] P. Klinkert, P. N. Post, P. J. Breslau, and J. H. van Bockel, “Saphenous vein versus PTFE for above-knee femoropopliteal bypass. A review of the literature,” *Eur. J. Vasc. Endovasc. Surg.*, vol. 27, no. 4, pp. 357–362, 2004, doi: 10.1016/j.ejvs.2003.12.027.

[3] D. C. Brewster, “Current controversies in the management of aortoiliac occlusive disease.,” *J. Vasc. Surg.*, vol. 25, no. 2, pp. 365–379, Feb. 1997, doi: 10.1016/s0741-5214(97)70359-8.

[4] J. Chlupác, E. Filová, and L. Bačáková, “Blood vessel replacement: 50 years of development and tissue engineering paradigms in vascular surgery,” *Physiol. Res.*, vol. 58, no. SUPPL.2, pp. 119–140, 2009.

[5] F. W. Hehrlein, M. Schlepper, F. Loskot, H. H. Scheld, P. Walter, and J. Mulch, “The use of expanded polytetrafluoroethylene (PTFE) grafts for myocardial revascularization.,” *J. Cardiovasc. Surg. (Torino).*, vol. 25, no. 6, pp. 549–553, 1984.

[6] S. Pashneh-Tala, S. MacNeil, and F. Claeyssens, “The tissue-engineered vascular graft - Past, present, and future,” *Tissue Eng. - Part B Rev.*, vol. 22, no. 1, pp. 68–100, 2016, doi: 10.1089/ten.teb.2015.0100.

[7] M. S. Baguneid, A. M. Seifalian, H. J. Salacinski, D. Murray, G. Hamilton, and M. G. Walker, “Tissue engineering of blood vessels,” *Br. J. Surg.*, vol. 93, no. 3, pp. 282–290, 2006, doi: 10.1002/bjs.5256.

[8] K. Torikai *et al.*, “A self-renewing, tissue-engineered vascular graft for arterial

reconstruction," *J. Thorac. Cardiovasc. Surg.*, vol. 136, no. 1, pp. 7–11, 2008, doi: 10.1016/j.jtcvs.2007.06.039.

[9] L. E. Niklason and R. S. Langer, "Advances in tissue engineering of blood vessels and other tissues," *Transpl. Immunol.*, vol. 5, no. 4, pp. 303–306, 1997, doi: 10.1016/S0966-3274(97)80013-5.

[10] Z. H. Syedain, L. A. Meier, J. W. Bjork, A. Lee, and R. T. Tranquillo, "Implantable arterial grafts from human fibroblasts and fibrin using a multi-graft pulsed flow-stretch bioreactor with noninvasive strength monitoring.," *Biomaterials*, vol. 32, no. 3, pp. 714–722, Jan. 2011, doi: 10.1016/j.biomaterials.2010.09.019.

[11] P. M. Crapo, T. W. Gilbert, and S. F. Badylak, "An overview of tissue and whole organ decellularization processes.," *Biomaterials*, vol. 32, no. 12, pp. 3233–3243, Apr. 2011, doi: 10.1016/j.biomaterials.2011.01.057.

[12] M. L. Wong, J. L. Wong, K. A. Athanasiou, and L. G. Griffiths, "Stepwise solubilization-based antigen removal for xenogeneic scaffold generation in tissue engineering," *Acta Biomater.*, vol. 9, no. 5, pp. 6492–6501, 2013, doi: 10.1016/j.actbio.2012.12.034.

[13] E. S. Chemla and M. Morsy, "Randomized clinical trial comparing decellularized bovine ureter with expanded polytetrafluoroethylene for vascular access," *Br. J. Surg.*, vol. 96, no. 1, pp. 34–39, 2009, doi: 10.1002/bjs.6434.

[14] M. Olausson *et al.*, "Transplantation of an allogeneic vein bioengineered with autologous stem cells: A proof-of-concept study," *Lancet*, vol. 380, no. 9838, pp. 230–237, 2012, doi: 10.1016/S0140-6736(12)60633-3.

[15] A. M. Woods, E. J. Rodenberg, M. C. Hiles, and F. M. Pavalko, "Improved biocompatibility of small intestinal submucosa (SIS) following conditioning by human

endothelial cells," *Biomaterials*, vol. 25, no. 3, pp. 515–525, 2004, doi: 10.1016/S0142-9612(03)00552-0.

[16] M. Peck, D. Gebhart, N. Dusserre, T. N. McAllister, and N. L'Heureux, "The evolution of vascular tissue engineering and current state of the art," *Cells Tissues Organs*, vol. 195, no. 1–2, pp. 144–158, 2011, doi: 10.1159/000331406.

[17] J. M. Kelm *et al.*, "A novel concept for scaffold-free vessel tissue engineering: Self-assembly of microtissue building blocks," *J. Biotechnol.*, vol. 148, no. 1, pp. 46–55, 2010, doi: 10.1016/j.jbiotec.2010.03.002.

[18] C. Norotte, F. S. Marga, L. E. Niklason, and G. Forgacs, "Scaffold-free vascular tissue engineering using bioprinting.," *Biomaterials*, vol. 30, no. 30, pp. 5910–5917, Oct. 2009, doi: 10.1016/j.biomaterials.2009.06.034.

[19] N. L'Heureux, S. Pâquet, R. Labbé, L. Germain, and F. A. Auger, "A completely biological tissue-engineered human blood vessel.," *FASEB J. Off. Publ. Fed. Am. Soc. Exp. Biol.*, vol. 12, no. 1, pp. 47–56, Jan. 1998, doi: 10.1096/fasebj.12.1.47.

[20] J. F. Woessner, "The determination of hydroxyproline in tissue and protein samples containing small proportions of this imino acid," *Arch. Biochem. Biophys.*, vol. 93, no. 2, pp. 440–447, 1961, doi: 10.1016/0003-9861(61)90291-0.

[21] K. Sugimoto *et al.*, "Matrix metalloproteinase promotes elastic fiber degradation in ligamentum flavum degeneration," *PLoS One*, vol. 13, no. 8, 2018, doi: 10.1371/journal.pone.0200872.

[22] M. L. Wong, J. K. Leach, K. A. Athanasiou, and L. G. Griffiths, "The role of protein solubilization in antigen removal from xenogeneic tissue for heart valve tissue engineering," *Biomaterials*, vol. 32, no. 32, pp. 8129–8138, 2011, doi:

10.1016/j.biomaterials.2011.07.030.

[23] D. R. Eyre, T. J. Koob, and K. P. Van Ness, “Quantitation of hydroxypyridinium crosslinks in collagen by high-performance liquid chromatography,” *Anal. Biochem.*, vol. 137, no. 2, pp. 380–388, 1984, doi: 10.1016/0003-2697(84)90101-5.

[24] H. A. Alturkistani, F. M. Tashkandi, and Z. M. Mohammedsaleh, “Histological Stains: A Literature Review and Case Study,” *Glob. J. Health Sci.*, vol. 8, no. 3, pp. 72–79, 2015, doi: 10.5539/gjhs.v8n3p72.

[25] G. Konig *et al.*, “Mechanical properties of completely autologous human tissue engineered blood vessels compared to human saphenous vein and mammary artery.,” *Biomaterials*, vol. 30, no. 8, pp. 1542–1550, Mar. 2009, doi: 10.1016/j.biomaterials.2008.11.011.

[26] D. Behrendt and P. Ganz, “Endothelial function: From vascular biology to clinical applications,” *Am. J. Cardiol.*, vol. 90, no. 10, Supplement 3, pp. L40–L48, 2002, doi: https://doi.org/10.1016/S0002-9149(02)02963-6.

[27] L. E. Niklason *et al.*, “Functional arteries grown in vitro,” *Science (80-.).*, vol. 284, no. 5413, pp. 489–493, 1999, doi: 10.1126/science.284.5413.489.

[28] G. Niu *et al.*, “Fluorescent imaging of endothelial cells in bioengineered blood vessels: the impact of crosslinking of the scaffold.,” *J. Tissue Eng. Regen. Med.*, vol. 10, no. 11, pp. 955–966, Nov. 2016, doi: 10.1002/term.1876.

[29] A. Alfonso-Garcia, C. Li, J. Bec, D. Yankelevich, L. Marcu, and B. Sherlock, “Fiber-based platform for synchronous imaging of endogenous and exogenous fluorescence of biological tissue,” *Opt. Lett.*, vol. 44, no. 13, p. 3350, 2019, doi: 10.1364/ol.44.003350.

[30] M. D. Slooter, A. Janssen, W. A. Bemelman, P. J. Tanis, and R. Hompes, “Currently

available and experimental dyes for intraoperative near-infrared fluorescence imaging of the ureters: a systematic review," *Tech. Coloproctol.*, vol. 23, no. 4, pp. 305–313, 2019, doi: 10.1007/s10151-019-01973-4.

[31] Z. Keidar, A. Engel, A. Hoffman, O. Israel, and S. Nitecki, "Prosthetic vascular graft infection: The role of 18F-FDG PET/CT," *J. Nucl. Med.*, vol. 48, no. 8, pp. 1230–1236, 2007, doi: 10.2967/jnumed.107.040253.

[32] S. Shahidi, A. Eskil, E. Lundof, A. Klærke, and B. S. Jensen, "Detection of Abdominal Aortic Graft Infection: Comparison of Magnetic Resonance Imaging and Indium-Labeled White Blood Cell Scanning," *Ann. Vasc. Surg.*, vol. 21, no. 5, pp. 586–592, 2007, doi: 10.1016/j.avsg.2007.03.018.

[33] E. I. Reinders Folmer *et al.*, "Diagnostic Imaging in Vascular Graft Infection: A Systematic Review and Meta-Analysis," *Eur. J. Vasc. Endovasc. Surg.*, vol. 56, no. 5, pp. 719–729, 2018, doi: 10.1016/j.ejvs.2018.07.010.

[34] D. A. Woodrum *et al.*, "Vascular wall elasticity measurement by magnetic resonance imaging," *Magn. Reson. Med.*, vol. 56, no. 3, pp. 593–600, 2006, doi: 10.1002/mrm.20991.

[35] L. A. Walton *et al.*, "Morphological characterisation of unstained and intact tissue micro-architecture by X-ray computed micro- and nano-tomography," *Sci. Rep.*, vol. 5, no. November 2014, pp. 1–14, 2015, doi: 10.1038/srep10074.

[36] P. N. T. Wells, "Ultrasound imaging," *Phys. Med. Biol.*, vol. 51, no. 13, 2006, doi: 10.1088/0031-9155/51/13/R06.

[37] N. Vanerio, M. Stijnen, B. A. J. M. de Mol, and L. M. Kock, "An Innovative Ex Vivo Vascular Bioreactor as Comprehensive Tool to Study the Behavior of Native Blood

Vessels Under Physiologically Relevant Conditions," *J. Eng. Sci. Med. Diagnostics Ther.*, vol. 2, no. 4, pp. 1–7, 2019, doi: 10.1115/1.4044472.

[38] A. Kole *et al.*, "Comparative Quantification of Arterial Lipid by Intravascular Photoacoustic-Ultrasound Imaging and Near-Infrared Spectroscopy-Intravascular Ultrasound," *J. Cardiovasc. Transl. Res.*, vol. 12, no. 3, pp. 211–220, 2019, doi: 10.1007/s12265-018-9849-2.

[39] K. Kim and W. R. Wagner, "Non-invasive and Non-destructive Characterization of Tissue Engineered Constructs Using Ultrasound Imaging Technologies: A Review," *Ann. Biomed. Eng.*, vol. 44, no. 3, pp. 621–635, 2016, doi: 10.1007/s10439-015-1495-0.

[40] K. P. Mercado, M. Helguera, D. C. Hocking, and D. Dalecki, "Estimating cell concentration in three-dimensional engineered tissues using high frequency quantitative ultrasound," *Ann. Biomed. Eng.*, vol. 42, no. 6, pp. 1292–1304, 2014, doi: 10.1007/s10439-014-0994-8.

[41] K. S. Rathod, S. M. Hamshere, D. A. Jones, and A. Mathur, "Intravascular Ultrasound Versus Optical Coherence Tomography for Coronary Artery Imaging - Apples and Oranges?," *Interv. Cardiol. Rev.*, vol. 10, no. 1, pp. 8–15, 2015, doi: 10.15420/icr.2015.10.1.8.

[42] S. L. Jacques, "Optical properties of biological tissues: a review.," *Phys. Med. Biol.*, vol. 58, no. 11, pp. R37-61, Jun. 2013, doi: 10.1088/0031-9155/58/11/R37.

[43] C. Balas, "Review of biomedical optical imaging - A powerful, non-invasive, non-ionizing technology for improving in vivo diagnosis," *Meas. Sci. Technol.*, vol. 20, no. 10, 2009, doi: 10.1088/0957-0233/20/10/104020.

[44] J. G. Fujimoto, C. Pitris, S. A. Boppart, and M. E. Brezinski, "Optical coherence

tomography: An emerging technology for biomedical imaging and optical biopsy," *Neoplasia*, vol. 2, no. 1–2, pp. 9–25, 2000, doi: 10.1038/sj.neo.7900071.

[45] C. M. Webb, E. Orion, D. P. Taggart, K. M. Channon, and C. Di Mario, "OCT imaging of aorto-coronary vein graft pathology modified by external stenting: 1-year post-surgery," *Eur. Heart J. Cardiovasc. Imaging*, vol. 17, no. 11, pp. 1290–1295, 2016, doi: 10.1093/ehjci/jev310.

[46] A. A. Gurjarpadhye *et al.*, "Imaging and characterization of bioengineered blood vessels within a bioreactor using free-space and catheter-based OCT," *Lasers Surg. Med.*, vol. 45, no. 6, pp. 391–400, 2013, doi: 10.1002/lsm.22147.

[47] X. Yu, R. Turcotte, F. Seta, and Y. Zhang, "Micromechanics of elastic lamellae: Unravelling the role of structural inhomogeneity in multi-scale arterial mechanics," *J. R. Soc. Interface*, vol. 15, no. 147, 2018, doi: 10.1098/rsif.2018.0492.

[48] R. Cicchi, N. Vogler, D. Kapsokalyvas, B. Dietzek, J. Popp, and F. S. Pavone, "From molecular structure to tissue architecture: Collagen organization probed by SHG microscopy," *J. Biophotonics*, vol. 6, no. 2, pp. 129–142, 2013, doi: 10.1002/jbio.201200092.

[49] B. M. Whited *et al.*, "Dynamic, Nondestructive Imaging of a Bioengineered Vascular Graft Endothelium," *PLoS One*, vol. 8, no. 4, 2013, doi: 10.1371/journal.pone.0061275.

[50] L. Bachmann, D. M. Zezell, A. da C. Ribeiro, L. Gomes, and A. S. Ito, "Fluorescence spectroscopy of biological tissues - A review," *Appl. Spectrosc. Rev.*, vol. 41, no. 6, pp. 575–590, 2006, doi: 10.1080/05704920600929498.

[51] D. Lorenser *et al.*, "Dual-modality needle probe for combined fluorescence imaging and three-dimensional optical coherence tomography," *Opt. Lett.*, vol. 38, no. 3, p. 266, Feb.

2013, doi: 10.1364/ol.38.000266.

[52] M. A. Yaseen, V. J. Srinivasan, I. Gorczynska, J. G. Fujimoto, D. A. Boas, and S. Sakadžić, “Multimodal optical imaging system for in vivo investigation of cerebral oxygen delivery and energy metabolism,” *Biomed. Opt. Express*, vol. 6, no. 12, p. 4994, 2015, doi: 10.1364/boe.6.004994.

[53] S. K. Nadkarni *et al.*, “Measurement of collagen and smooth muscle cell content in atherosclerotic plaques using polarization-sensitive optical coherence tomography,” *J. Am. Coll. Cardiol.*, vol. 49, no. 13, p. 1474—1481, Apr. 2007, doi: 10.1016/j.jacc.2006.11.040.

[54] C. Sun, B. Standish, and V. X. D. Yang, “Optical coherence elastography: current status and future applications,” *J. Biomed. Opt.*, vol. 16, no. 4, p. 043001, 2011, doi: 10.1117/1.3560294.

[55] K. P. Quinn *et al.*, “Optical metrics of the extracellular matrix predict compositional and mechanical changes after myocardial infarction,” *Sci. Rep.*, vol. 6, no. June, pp. 1–12, 2016, doi: 10.1038/srep35823.

[56] T. A. Shaik *et al.*, “FLIm-Guided Raman Imaging to Study Cross-Linking and Calcification of Bovine Pericardium,” *Anal. Chem.*, vol. 92, no. 15, pp. 10659–10667, 2020, doi: 10.1021/acs.analchem.0c01772.

[57] A. H. Hill and D. Fu, “Cellular Imaging Using Stimulated Raman Scattering Microscopy,” *Anal. Chem.*, vol. 91, no. 15, pp. 9333–9342, 2019, doi: 10.1021/acs.analchem.9b02095.

[58] W. Lewis, J. P. Padilla-Martinez, A. Ortega-Martinez, and W. Franco, “Changes in endogenous UV fluorescence and biomechanical stiffness of bovine articular cartilage after collagenase digestion are strongly correlated,” *J. Biophotonics*, vol. 10, no. 8, pp.

1018–1025, 2017, doi: 10.1002/jbio.201600093.

[59] L. Marcu, “Fluorescence lifetime in cardiovascular diagnostics,” *J. Biomed. Opt.*, vol. 15, pp. 11106–11110, 2010, doi: 10.1117/1.3327279.

[60] H. B. Manning *et al.*, “Detection of cartilage matrix degradation by autofluorescence lifetime,” *Matrix Biol.*, vol. 32, no. 1, pp. 32–38, 2013, doi: 10.1016/j.matbio.2012.11.012.

[61] D. R. Yankelevich *et al.*, “Design and evaluation of a device for fast multispectral time-resolved fluorescence spectroscopy and imaging,” *Rev. Sci. Instrum.*, vol. 85, no. 3, 2014, doi: 10.1063/1.4869037.

[62] C. Li *et al.*, “Label-Free Assessment of Collagenase Digestion on Bovine Pericardium Properties by Fluorescence Lifetime Imaging,” *Ann. Biomed. Eng.*, vol. 46, no. 11, pp. 1870–1881, 2018, doi: 10.1007/s10439-018-2087-6.

[63] J. Liu, Y. Sun, J. Qi, and L. Marcu, “A novel method for fast and robust estimation of fluorescence decay dynamics using constrained least-squares deconvolution with Laguerre expansion,” *Phys. Med. Biol.*, vol. 57, no. 4, pp. 843–865, Feb. 2012, doi: 10.1088/0031-9155/57/4/843.

[64] E. Filova *et al.*, “Collagen structures in pericardium and aortic heart valves and their significance for tissue engineering,” *2013 E-Health Bioeng. Conf. EHB 2013*, no. February 2015, 2013, doi: 10.1109/EHB.2013.6707382.

[65] M. L. Wong, J. L. Wong, R. M. Horn, K. C. Sannajust, D. A. Rice, and L. G. Griffiths, “Effect of Urea and Thiourea on Generation of Xenogeneic Extracellular Matrix Scaffolds for Tissue Engineering,” *Tissue Eng. - Part C Methods*, vol. 22, no. 7, pp. 700–707, 2016, doi: 10.1089/ten.tec.2015.0552.

[66] D. S. Elson, J. A. Jo, and L. Marcu, “Miniaturized side-viewing imaging probe for fluorescence lifetime imaging (FLIM): Validation with fluorescence dyes, tissue structural proteins and tissue specimens,” *New J. Phys.*, vol. 9, 2007, doi: 10.1088/1367-2630/9/5/127.

[67] J. E. Phipps, Y. Sun, M. C. Fishbein, and L. Marcu, “A fluorescence lifetime imaging classification method to investigate the collagen to lipid ratio in fibrous caps of atherosclerotic plaque,” *Lasers Surg. Med.*, vol. 44, no. 7, pp. 564–571, 2012, doi: 10.1002/lsm.22059.

[68] V. Lutz, M. Sattler, S. Gallinat, H. Wenck, R. Poertner, and F. Fischer, “Impact of collagen crosslinking on the second harmonic generation signal and the fluorescence lifetime of collagen autofluorescence,” *Ski. Res. Technol.*, vol. 18, no. 2, pp. 168–179, 2012, doi: 10.1111/j.1600-0846.2011.00549.x.

[69] A. S. Duarte, A. Correia, and A. C. Esteves, “Bacterial collagenases - A review,” *Crit. Rev. Microbiol.*, vol. 42, no. 1, pp. 106–126, 2016, doi: 10.3109/1040841X.2014.904270.

[70] G. Jones, W. R. Jackson, C. Y. Choi, and W. R. Bergmark, “Solvent effects on emission yield and lifetime for coumarin laser dyes. Requirements for a rotatory decay mechanism,” *J. Phys. Chem.*, vol. 89, no. 2, pp. 294–300, 1985, doi: 10.1021/j100248a024.

[71] K. Bilodeau, F. Couet, F. Boccafoschi, and D. Mantovani, “Thoughts and Progress: Design of a Perfusion Bioreactor Specific to the Regeneration of Vascular Tissue Under Mechanical tresses,” *Artif. Organs*, vol. 29, no. December 2004, pp. 906–922, 2005.

[72] I. Martin, D. Wendt, and M. Heberer, “The role of bioreactors in tissue engineering,” *Trends Biotechnol.*, vol. 22, no. 2, pp. 80–86, 2004, doi: 10.1016/j.tibtech.2003.12.001.

[73] J. P. Stegemann and R. M. Nerem, “Phenotype modulation in vascular tissue engineering using biochemical and mechanical stimulation,” *Ann. Biomed. Eng.*, vol. 31, no. 4, pp. 391–402, 2003, doi: 10.1114/1.1558031.

[74] D. Seliktar, R. M. Nerem, and Z. S. Galis, “Mechanical strain-stimulated remodeling of tissue-engineered blood vessel constructs,” *Tissue Eng.*, vol. 9, no. 4, pp. 657–666, 2003, doi: 10.1089/107632703768247359.

[75] V. Barron, E. Lyons, C. Stenson-Cox, P. E. McHugh, and A. Pandit, “Bioreactors for Cardiovascular Cell and Tissue Growth: A Review,” *Ann. Biomed. Eng.*, vol. 31, no. 9, pp. 1017–1030, 2003, doi: 10.1114/1.1603260.

[76] Z. X. Zhang *et al.*, “Design of a novel bioreactor and application in vascular tissue engineering,” *Appl. Surf. Sci.*, vol. 255, no. 2, pp. 541–544, 2008, doi: 10.1016/j.apsusc.2008.06.177.

[77] C. Li *et al.*, “Simultaneous intraluminal imaging of tissue autofluorescence and eGFP-labeled cells in engineered vascular grafts inside a bioreactor,” *Methods Appl. Fluoresc.*, vol. 7, no. 4, 2019, doi: 10.1088/2050-6120/ab4342.

[78] M. E. Mertens *et al.*, “USPIO-labeled textile materials for non-invasive MR imaging of tissue-engineered vascular grafts,” *Biomaterials*, vol. 39, pp. 155–163, 2015, doi: 10.1016/j.biomaterials.2014.10.076.

[79] A. A. Appel, M. A. Anastasio, J. C. Larson, and E. M. Brey, “Imaging challenges in biomaterials and tissue engineering.,” *Biomaterials*, vol. 34, no. 28, pp. 6615–6630, Sep. 2013, doi: 10.1016/j.biomaterials.2013.05.033.

[80] W. Chen *et al.*, “In vitro remodeling and structural characterization of degradable polymer scaffold-based tissue-engineered vascular grafts using optical coherence tomography,”

Cell Tissue Res., vol. 370, no. 3, pp. 417–426, 2017, doi: 10.1007/s00441-017-2683-z.

[81] K. Nishimiya *et al.*, "Micro-Optical Coherence Tomography for Endothelial Cell Visualization in the Coronary Arteries.," *JACC. Cardiovascular imaging*, vol. 12, no. 9. pp. 1878–1880, Sep. 2019, doi: 10.1016/j.jcmg.2019.01.021.

[82] A. Alfonso-Garcia, J. Shklover, B. E. Sherlock, A. Panitch, L. G. Griffiths, and L. Marcu, "Fiber-based fluorescence lifetime imaging of recellularization processes on vascular tissue constructs," *J. Biophotonics*, 2018, doi: 10.1002/jbio.201700391.

[83] L. Song *et al.*, "Successful development of small diameter tissue-engineering vascular vessels by our novel integrally designed pulsatile perfusion-based bioreactor," *PLoS One*, vol. 7, no. 8, 2012, doi: 10.1371/journal.pone.0042569.

[84] M. S. Hahn, M. K. McHale, E. Wang, R. H. Schmedlen, and J. L. West, "Physiologic pulsatile flow bioreactor conditioning of poly(ethylene glycol)-based tissue engineered vascular grafts," *Ann. Biomed. Eng.*, vol. 35, no. 2, pp. 190–200, 2007, doi: 10.1007/s10439-006-9099-3.

[85] P. Wahl, J. C. Auchet, A. J. W. G. Visser, and F. Müller, "Time resolved fluorescence of flavin adenine dinucleotide," *FEBS Lett.*, vol. 44, no. 1, pp. 67–70, 1974, doi: https://doi.org/10.1016/0014-5793(74)80307-8.

[86] J. R. Lakowicz, H. Szmacinski, K. Nowaczyk, and M. L. Johnson, "Fluorescence lifetime imaging of free and protein-bound NADH," *Proc. Natl. Acad. Sci. U. S. A.*, vol. 89, no. 4, pp. 1271–1275, Feb. 1992, doi: 10.1073/pnas.89.4.1271.

[87] D. Magde, G. E. Rojas, and P. G. Seybold, "Solvent Dependence of the Fluorescence Lifetimes of Xanthene Dyes," *Photochem. Photobiol.*, vol. 70, no. 5, pp. 737–744, Nov. 1999, doi: 10.1111/j.1751-1097.1999.tb08277.x.

[88] Z. Z. Liu, M. L. Wong, and L. G. Griffiths, “Effect of bovine pericardial extracellular matrix scaffold niche on seeded human mesenchymal stem cell function,” *Sci. Rep.*, vol. 6, no. October, pp. 1–12, 2016, doi: 10.1038/srep37089.

[89] B. E. Sherlock *et al.*, “Nondestructive assessment of collagen hydrogel cross-linking using time-resolved autofluorescence imaging,” *J. Biomed. Opt.*, vol. 23, no. 03, p. 1, 2018, doi: 10.1117/1.jbo.23.3.036004.

[90] D. Ma, J. Bec, D. R. Yankelevich, D. Gorpas, H. Fatakdawala, and L. Marcu, “Rotational multispectral fluorescence lifetime imaging and intravascular ultrasound: bimodal system for intravascular applications,” *J. Biomed. Opt.*, vol. 19, no. 6, p. 066004, 2014, doi: 10.1117/1.jbo.19.6.066004.

[91] L. Scolaro *et al.*, “Molecular imaging needles: dual-modality optical coherence tomography and fluorescence imaging of labeled antibodies deep in tissue,” *Biomed. Opt. Express*, vol. 6, no. 5, p. 1767, 2015, doi: 10.1364/boe.6.001767.

[92] J. Li *et al.*, “Two-photon polymerisation 3D printed freeform micro-optics for optical coherence tomography fibre probes,” *Sci. Rep.*, vol. 8, no. 1, pp. 1–9, 2018, doi: 10.1038/s41598-018-32407-0.

[93] D. C. Adams, Y. Wang, L. P. Hariri, and M. J. Suter, “Advances in endoscopic optical coherence tomography catheter designs,” *IEEE J. Sel. Top. Quantum Electron.*, vol. 22, no. 3, pp. 210–221, 2016, doi: 10.1109/JSTQE.2015.2510295.

[94] F. Wolf *et al.*, “MR and PET-CT monitoring of tissue-engineered vascular grafts in the ovine carotid artery,” *Biomaterials*, vol. 216, p. 119228, 2019, doi: https://doi.org/10.1016/j.biomaterials.2019.119228.

[95] R. Puri, M. I. Worthley, and S. J. Nicholls, “Intravascular imaging of vulnerable coronary

plaque: Current and future concepts," *Nat. Rev. Cardiol.*, vol. 8, no. 3, pp. 131–139, 2011, doi: 10.1038/nrcardio.2010.210.

[96] P. Libby, P. M. Ridker, and A. Maseri, "Inflammation and atherosclerosis," *Circulation*, vol. 105, no. 9, pp. 1135–1143, 2002, doi: 10.1161/hc0902.104353.

[97] K. K. Shung, "High Frequency Ultrasonic Imaging," *J. Med. Ultrasound*, vol. 17, no. 1, pp. 25–30, 2009, doi: 10.1016/S0929-6441(09)60012-6.

[98] G. S. Mintz *et al.*, "American College of Cardiology clinical expert consensus document on standards for acquisition, measurement and reporting of intravascular ultrasound studies (IVUS)," *J. Am. Coll. Cardiol.*, vol. 37, no. 5, pp. 1478–1492, 2001, doi: 10.1016/S0735-1097(01)01175-5.

[99] T. Kubo *et al.*, "OCT compared with IVUS in a coronary lesion assessment: The OPUS-CLASS study," *JACC Cardiovasc. Imaging*, vol. 6, no. 10, pp. 1095–1104, 2013, doi: 10.1016/j.jcmg.2013.04.014.

[100] G. J. Tearney *et al.*, "Consensus standards for acquisition, measurement, and reporting of intravascular optical coherence tomography studies: A report from the International Working Group for Intravascular Optical Coherence Tomography Standardization and Validation," *J. Am. Coll. Cardiol.*, vol. 59, no. 12, pp. 1058–1072, 2012, doi: 10.1016/j.jacc.2011.09.079.

[101] H. Yoo *et al.*, "Intra-arterial catheter for simultaneous microstructural and molecular imaging in vivo," *Nat. Med.*, vol. 17, no. 12, pp. 1680–1684, 2011, doi: 10.1038/nm.2555.

[102] S. Kim, H. Yoo, and J. W. Kim, "Long Journey of Intravascular Imaging," *JACC Cardiovasc. Imaging*, 2020, doi: 10.1016/j.jcmg.2020.11.015.

[103] G. J. Ughi *et al.*, "Clinical Characterization of Coronary Atherosclerosis With Dual-

Modality OCT and Near-Infrared Autofluorescence Imaging," *JACC Cardiovasc. Imaging*, vol. 9, no. 11, pp. 1304–1314, 2016, doi: 10.1016/j.jcmg.2015.11.020.

[104] J. Bec *et al.*, "In vivo label-free structural and biochemical imaging of coronary arteries using an integrated ultrasound and multispectral fluorescence lifetime catheter system," *Sci. Rep.*, vol. 7, no. 1, pp. 1–9, 2017, doi: 10.1038/s41598-017-08056-0.

[105] J. Bec *et al.*, "Label-Free Visualization and Quantification of Biochemical Markers of Atherosclerotic Plaque Progression Using Intravascular Fluorescence Lifetime," *JACC Cardiovasc. Imaging*, 2020, doi: 10.1016/j.jcmg.2020.10.004.

[106] K. O. Kuku *et al.*, "Near-Infrared Spectroscopy Intravascular Ultrasound Imaging: State of the Art," *Front. Cardiovasc. Med.*, vol. 7, no. June, 2020, doi: 10.3389/fcvm.2020.00107.

[107] X. Chen, W. Kim, M. J. Serafino, Z. Tan, J. A. Jo, and B. E. Applegate, "Dual-modality optical coherence tomography and frequency-domain fluorescence lifetime imaging microscope system for intravascular imaging," *J. Biomed. Opt.*, vol. 25, no. 09, p. 096010, Sep. 2020, doi: 10.1117/1.JBO.25.9.096010.

[108] X. Li *et al.*, "Integrated IVUS-OCT Imaging for Atherosclerotic Plaque Characterization," *IEEE J. Sel. Top. Quantum Electron.*, vol. 20, no. 2, 2014, doi: 10.1109/JSTQE.2013.2274724.

[109] M. W. Lee *et al.*, "Comprehensive intravascular imaging of atherosclerotic plaque in vivo using optical coherence tomography and fluorescence lifetime imaging," *Sci. Rep.*, vol. 8, no. 1, p. 14561, Sep. 2018, doi: 10.1038/s41598-018-32951-9.

[110] E. Rothstein, H. Aronow, B. M. Hawkins, and M. N. Young, "Intravascular Imaging for Peripheral Vascular Disease and Endovascular Intervention," *Curr. Cardiovasc. Imaging*

Rep., vol. 13, no. 2, 2020, doi: 10.1007/s12410-020-9526-0.

[111] J. E. Phipps *et al.*, "Macrophages and intravascular OCT bright spots: A quantitative study," *JACC Cardiovasc. Imaging*, vol. 8, no. 1, pp. 63–72, 2015, doi: 10.1016/j.jcmg.2014.07.027.

[112] M. G. Hyeon, H.-J. Kim, B.-M. Kim, and T. J. Eom, "Spectral domain optical coherence tomography with balanced detection using single line-scan camera and optical delay line," *Opt. Express*, vol. 23, no. 18, p. 23079, 2015, doi: 10.1364/oe.23.023079.

[113] J. Bec, C. Li, and L. Marcu, "Broadband, freeform focusing micro-optics for a side-viewing imaging catheter," *Opt. Lett.*, vol. 44, no. 20, p. 4961, 2019, doi: 10.1364/ol.44.004961.

[114] H. M. Lopera and L. G. Griffiths, "Antigen removal process preserves function of small diameter venous valved conduits, whereas SDS-decellularization results in significant valvular insufficiency," *Acta Biomater.*, vol. 107, pp. 115–128, 2020, doi: 10.1016/j.actbio.2020.03.003.

[115] W. Kim, X. Chen, J. A. Jo, and B. E. Applegate, "Lensless, ultra-wideband fiber optic rotary joint for biomedical applications," *Opt. Lett.*, vol. 41, no. 9, p. 1973, May 2016, doi: 10.1364/ol.41.001973.

[116] M. J. Gora, M. J. Suter, G. J. Tearney, and X. Li, "Endoscopic optical coherence tomography: technologies and clinical applications [Invited]," *Biomed. Opt. Express*, vol. 8, no. 5, p. 2405, 2017, doi: 10.1364/boe.8.002405.

[117] F. O. Obiweluozor *et al.*, "Considerations in the Development of Small-Diameter Vascular Graft as an Alternative for Bypass and Reconstructive Surgeries: A Review," *Cardiovasc. Eng. Technol.*, vol. 11, no. 5, pp. 495–521, 2020, doi: 10.1007/s13239-020-

00482-y.

Work published in referred journals

[1] **Li, C.**, Shklover, J., Parvizi, M., Sherlock, B. E., Alfonso Garcia, A., Haudenschild, A. K., Griffiths, L. G., Marcu, L. (2018). Label-Free Assessment of Collagenase Digestion on Bovine Pericardium Properties by Fluorescence Lifetime Imaging. Annals of Biomedical Engineering, 46(11), 1870–1881.

[2] Alfonso-Garcia, A., **Li, C.**, Bec, J., Yankelevich, D., Marcu, L., Sherlock, B. (2019). Fiber-based platform for synchronous imaging of endogenous and exogenous fluorescence of biological tissue. Optics Letters, 44(13), 3350.

[3] Bec, J., **Li, C.**, Marcu, L. (2019). Broadband, freeform focusing micro-optics for a side-viewing imaging catheter. Optics Letters, 44(20), 4961.

[4] **Li, C.**, Alfonso-Garcia, A., McMasters, J., Bec, J., Weyers, B., Uyesaka, L., Griffiths, L., Panitch, A., Marcu, L. (2019). Simultaneous intraluminal imaging of tissue autofluorescence and eGFP-labeled cells in engineered vascular grafts inside a bioreactor. Methods and Applications in Fluorescence, 7(4).

[5] Sherlock, B. E., **Li, C.**, Zhou, X., Alfonso-Garcia, A., Bec, J., Yankelevich, D., Marcu, L. (2019). Multiscale, multispectral fluorescence lifetime imaging using a double-clad fiber. Optics Letters, 44(9), 2302.

[6] Harvestine, J. N., Sheaff, C. S., **Li, C.**, Haudenschild, A. K., Gionet-Gonzales, M. A., Hu, J. C., Athanasiou, K. A., Marcu, L., Leach, J. K. (2019). Multimodal label-free imaging for detecting maturation of engineered osteogenic grafts. ACS Biomaterials Science Engineering.